

1 **Increasing precipitation due to climate change could partially**  
2 **offset the impact of warming on glacier loss in the monsoon-**  
3 **influenced Himalaya until 2100 CE**

4 Anya M. Schlich-Davies<sup>1\*</sup>, Ann V. Rowan<sup>2\*</sup>, Andrew N. Ross<sup>1</sup>, Duncan J. Quincey<sup>3</sup>, Vivi K.  
5 Pedersen<sup>4</sup>

6  
7  
8 <sup>1</sup>Priestley International Centre for Climate, School of Earth and Environment, University of Leeds,  
9 UK

10 <sup>2</sup>Department of Earth Science, University of Bergen and Bjerknes Centre for Climate Research,  
11 Bergen, Norway

12 <sup>3</sup>School of Geography, University of Leeds, UK

13 <sup>4</sup>Department of Geoscience, Aarhus University, Aarhus C, Denmark

14  
15 \*These authors contributed equally to this work

16  
17 Correspondence to: Ann V. Rowan ([ann.rowan@uib.no](mailto:ann.rowan@uib.no))

18  
19  
20 **Abstract.** Glacier mass in the Himalaya is projected to shrink by 53–70% due to climate change by  
21 2100 CE. However, the impact of changes in precipitation amount and distribution on future glacier  
22 change remains uncertain because these variables are not often represented in glacier model projections.  
23 We explored the combined effects of past and future changes in air temperature and precipitation  
24 amount and distribution on the evolution of Khumbu Glacier in the Everest region of Nepal. We used a  
25 glacier modelling approach that forced an ice-dynamical glacier evolution model with surface mass  
26 balance calculations that included mesoscale meteorological variables derived from statistical  
27 downscaling of existing regional climate projections. Our simulations show that historical warming has  
28 committed Khumbu Glacier to mass loss of 10–23% during this century, and that under an intermediate  
29 future emissions scenario (RCP4.5), this glacier could lose 70% mass by 2100 CE due to warming. The  
30 projected increase in precipitation in tandem with warming could offset about half of the projected  
31 glacier loss, such that the total decrease in glacier mass by 2100 CE compared to the present day would  
32 be reduced to 34%. However, under a higher future emissions scenario (RCP8.5) glacier loss due to  
33 warming will not be compensated by changes in precipitation, but will instead result in substantial  
34 ablation above 6,000 m elevation, with devastating consequences for one of the highest glaciers on  
35 Earth.

36  
37 **1. Introduction**

38 Projecting glacier change in response to climate change is important for determining the impact of  
39 anthropogenic warming on regional water availability (Pritchard, 2019). High Mountain Asia is  
40 projected to lose 34 ± 19% of glacier mass by 2100 CE if warming is limited to 1.5°C to meet the  
41 ambitious Paris Agreement target (Kraaijenbrink et al., 2017). Less ambitious projections give 53 ±  
42 23% glacier mass loss by 2100 CE under the intermediate emissions scenario RCP4.5, and 69 ± 20%  
43 under the high emissions scenario RCP8.5 (Kraaijenbrink et al., 2017; Marzeion et al., 2020; Rounce  
44 et al., 2023). Such projections are challenging to make, because accumulation and ablation processes  
45 in mountain environments are driven by orographic feedbacks between high-relief topography and  
46 atmospheric circulation systems such as the South Asian Summer Monsoon (e.g., Bookhagen and  
47 Burbank, 2006). Furthermore, large uncertainties arise from the challenge of simulating the interactions  
48 between the mass balance regimes of monsoon-influenced glaciers, where accumulation and ablation  
49 both occur during the monsoon season, and the dynamics of glaciers flowing through high-relief  
50 topography that includes processes such as the development of supraglacial debris layers that modify  
51 surface melting (Dehecq et al., 2019; Miles et al., 2018b; Salerno et al., 2023). Variability in the extent  
52 and intensity of the Indian Summer Monsoon during the Last Glacial Maximum was shown to affect  
53 glacier expansion in the monsoon-influenced Himalaya through changes in snowfall distribution (Benn

Deleted: is

Deleted: is

56 and Owen, 1998; Owen et al., 2009). Future Indian Summer Monsoon precipitation and variability  
57 projected in Global Circulation Models (GCMs) will increase with current global warming  
58 (Katzenberger et al., 2021), but as yet, the effect of projected changes in precipitation amount, timing,  
59 and phase (rain/snow) on Himalayan glaciers remain poorly constrained (Immerzeel et al., 2012; Mölg  
60 et al., 2014; Ragetti et al., 2016; Shaw et al., 2022; Shea et al., 2015).

61  
62 Supraglacial debris covers 4–7% of glacier surfaces globally and 30% of glacier ablation areas in the  
63 Himalaya, and modifies the response of glaciers to climate change relative to regional trends (Herreid  
64 and Pellicciotti, 2020; Kraaijenbrink et al., 2017; Rounce et al., 2023; Rowan et al., 2015). Satellite  
65 observations show that the rate of glacier mass loss across the Himalaya has accelerated over the last  
66 40 years for both clean-ice glaciers and debris-covered glaciers (Maurer et al., 2019). Observations and  
67 modelling studies indicate that thick supraglacial debris caused historical mass loss from debris-covered  
68 glaciers to lag that of clean-ice glaciers, such that debris-covered glaciers are currently larger than would  
69 otherwise be the case (King et al., 2020; Rounce et al., 2023; Rowan et al., 2021). However, the  
70 dampening effect of supraglacial debris on glacier mass loss is overturned by the development of  
71 extensive supraglacial ponds and ice cliffs within debris layers (Miles et al., 2018a; Strickland et al.,  
72 2023) and the stagnation and detachment of debris-covered tongues from the upper and more active  
73 sections of these glaciers (Rowan et al., 2021). Quantifying the impact of feedbacks set up by the  
74 formation and expansion of supraglacial debris layers at a regional scale requires exploring such  
75 processes at scales that can be resolved in ice-dynamical glacier evolution models (Rowan et al., 2015;  
76 Nicholson et al., 2021; Compagno et al., 2022). These processes can be considered in 2-D (along the  
77 glacier flowline) either considering stochastic debris delivery to the glacier (Vacca et al., 2010) or  
78 continuous debris delivery, which can result in the over-accumulation of debris at the terminus  
79 (Anderson and Anderson, 2016; Ferguson and Vieli, 2020; Jouvett et al., 2011), or in 3-D (using the  
80 horizontal and vertical ice-flow fields), which simulates the lateral transport and deposition of debris to  
81 the margins of the ablation area (Rowan et al., 2015; Wirbel et al., 2018). While recent rapid warming  
82 has resulted in a rise in regional equilibrium line altitude (ELA) and caused recession and collapse of  
83 glacier termini for both clean-ice glaciers and debris-covered glaciers (King et al., 2020), the decay of  
84 the former ablation areas of debris-covered glaciers is delayed by supraglacial debris, such that the  
85 terminus of the actively flowing glacier can remain in contact with the stagnant former ice tongue rather  
86 than separating (Maurer et al., 2019; Pellicciotti et al., 2015; Rowan et al., 2021).

87  
88 In common with most large debris-covered Himalayan glaciers, Khumbu Glacier in the Everest region  
89 of Nepal (Fig. 1) is in greater imbalance with climate than a climatically equivalent clean-ice glacier,  
90 and has maintained a more extensive ice volume than would be possible without supraglacial debris  
91 (Rowan et al., 2021). Khumbu Glacier (RGI2000-v7.0-G-15-08331) is 16.0 km long with an area of  
92 26.4 km<sup>2</sup>. The median glacier elevation is 6,025 m a.s.l. from the terminus at 4,879 m a.s.l. to the  
93 headwall at 7,981 m a.s.l. (RGI 7.0 Consortium, 2023). The stagnant debris-covered tongue has an area  
94 of 6.2 km<sup>2</sup> (23% of the total glacier). As a result of reduced ice flux from the accumulation area, the  
95 debris-covered tongue no longer receives much (or any) input of ice, and has dynamically detached  
96 from the active glacier (Fig. 1C); this observation is confirmed by the rapid reduction in ice flow and  
97 the peak in glacier surface lowering below the Khumbu Icefall where the debris layer is thinnest (King  
98 et al., 2020; Quincey et al., 2009). Observations and modelling of the dynamics and structure show that  
99 the tongue for 5 km upglacier from the terminus (25% of the total length, 20% of total ice volume) is  
100 stagnant and dynamically detached from the active glacier in the last century (Miles et al., 2022;  
101 Quincey et al., 2009; Rowan et al., 2021). Basal ice at the glacier surface indicates that the active  
102 terminus overrides the stagnant glacier tongue (Miles et al., 2021) and measurements of surface  
103 displacement show no longitudinal flow through the detached debris-covered tongue, which is  
104 collapsing laterally at a rate of about 3 m a<sup>-1</sup> (Watson et al., 2017). Therefore, the active glacier and the  
105 stagnant debris-covered tongue evolve along different trajectories, and only the part of Khumbu Glacier  
106 above the terminus of the active glacier can be considered dynamic (Miles et al., 2022). Projections of  
107 future glacier evolution should therefore discount the heavily debris-covered former tongue, which is  
108 decaying *in situ* without any input of new ice from the accumulation area, while considering the  
109 development of supraglacial debris across the ablation area of the active glacier.  
110

Deleted: ¶  
¶

Deleted: detached

Deleted: Howe

Deleted: er, a

Moved (insertion) [1]

Deleted: of Khumbu Glacier

Deleted: ¶

Deleted: will

Deleted: ¶

120 We applied a novel glacier modelling approach to Khumbu Glacier to test the hypothesis that changes  
121 in precipitation in response to climate change will reduce the impact of warming on glacier mass loss.  
122 Khumbu Glacier is a benchmark debris-covered glacier in the monsoon-influenced Himalaya flowing  
123 from 7,981 m above sea level (a.s.l.) to 4,879 m a.s.l. that is representative in terms of elevation of the  
124 majority of glaciers in the Central and Eastern Himalaya (Fig. 1B). The ‘Little Ice Age’ (LIA) maximum  
125 of Khumbu Glacier occurred about 200–500 years before present, which is consistent with ages  
126 produced for moraines elsewhere in the central Himalaya (Hornsey et al., 2022; Rowan, 2017). Khumbu  
127 Glacier was slightly larger than today during the late Holocene, transitioning from a clean-ice glacier  
128 with high velocities and efficient export of debris to a debris-covered glacier with lower velocities after  
129 the LIA; this change was initiated by the reduction in ice flux to the glacier tongue promoted by a rise  
130 in ELA (Rowan et al., 2015). We used a 3-D ice-flow model forced by mass balance calculated from  
131 mesoscale meteorological variables to simulate the evolution of Khumbu Glacier from the late  
132 Holocene (~1 ka) through the present day (2015 CE) until 2100 CE using results from three downscaled  
133 Regional Climate Models (RCMs) under two Relative Concentration Pathways (RCPs). This approach  
134 represents an advance in the use of such models to understand the evolution of Himalayan glaciers  
135 whereby mesoscale meteorological forcing of surface mass balance is used with a thermomechanical  
136 glacier model to represent the processes of sublimation, snow avalanching, and debris transport, all of  
137 which are important controls on the mass balance of Himalayan glaciers (Kneib et al., 2025).  
138 Simulations start from the late Holocene when Khumbu Glacier was last in dynamic equilibrium with  
139 the local climate, as evidenced by large ice-marginal moraines dated to  $1.3 \pm 0.1$  ka surrounding the  
140 present-day glacier (Hornsey et al., 2022), and when the glacier surface was free of debris (Rowan et  
141 al., 2015).  
142

## 143 2. Methods

### 144 2.1 Glacier model experimental design

145 The glacier model experiments used mesoscale meteorological variables to calculate surface mass  
146 balance for the Khumbu Glacier catchment in combination with a debris-covered glacier evolution  
147 model to represent the surface processes that modify mass balance (Fig. 2A). Our approach produced a  
148 total of six simulations of Khumbu Glacier to 2100 CE from three CORDEX South Asia region RCMs  
149 (NOAA, CCCma, IPSL; Lutz et al., 2016) under two RCPs (RCP4.5 and RCP8.5; Collins et al., 2013)  
150 to explore the impacts of possible variability in future precipitation amount and distribution in tandem  
151 with warming on glacier evolution. Before we used the RCMs to force the future climate scenarios, we  
152 evaluated their capabilities against observations of present-day weather and climate. The experimental  
153 design represents an advance compared with previous glacier modelling efforts by including in each  
154 simulation; (1) mesoscale meteorological phenomena, including sublimation, (2) the redistribution of  
155 surface mass by snow avalanching, and (3) the feedbacks between debris transport, ice flow and mass  
156 balance. This section describes the experimental design for the glacier modelling workflow,  
157 downscaling of the present-day RCMs using meteorological data from automatic weather stations  
158 (AWS) in the Khumbu Valley, downscaling of the future RCMs for both RCPs, the surface energy and  
159 mass balance calculations using COSIPY (Sauter et al., 2020) and the debris-covered glacier evolution  
160 modelling using iSOSIA (Rowan et al., 2015). A reference simulation and sensitivity experiments were  
161 carried out for the period 2013–2015 CE, and the simulations of future glacier change represented the  
162 period 2015–2100 CE. Additional information about the development and testing of the modelling  
163 approach is provided in Appendix A.  
164  
165

166 The spin-up simulation from the ice-free model domain to represent the late Holocene glacier was  
167 forced using a simple approximation of mass balance. The ice-free model domain was found by  
168 subtracting the estimated ice thickness (Farinotti et al., 2019) from a 30-m digital elevation model  
169 (DEM) acquired from the Shuttle Radar Topography Mission (Farr et al., 2007). The ice-free model  
170 domain incorporated the full hydrological catchment including the steep hillslopes in the Western Cwm  
171 that provide snow to the glacier surface by avalanching. As a starting point for our transient simulations  
172 of Khumbu Glacier, we reconstructed the late Holocene glacier from the ice-free domain using an ELA  
173 of 5,325 m a.s.l. and an atmospheric lapse rate of  $-4.0^\circ\text{C km}^{-1}$  in a 5,000 year simulation. Accumulation  
174 above the ELA was calculated as a function of elevation  $0.2 \text{ m m}^{-1}$  up to a maximum of  $2.0 \text{ m w.e. a}^{-1}$

**Moved up [1]:** Observations and modelling of the dynamics and structure of Khumbu Glacier show that the tongue for 5 km upglacier from the terminus (25% of the total length, 20% of total ice volume) is stagnant and dynamically detached from the active glacier in the last century (Miles et al., 2022; Quincey et al., 2009; Rowan et al., 2021). Basal ice at the glacier surface indicates that the active terminus overrides the stagnant glacier tongue (Miles et al., 2021) and measurements of surface displacement show no longitudinal flow through the detached debris-covered tongue, which is collapsing laterally at a rate of about  $3 \text{ m a}^{-1}$  (Watson et al., 2017).<sup>4</sup>

**Deleted:** Khumbu Glacier (RGI2000-v7.0-G-15-08331) is 16.0 km long with an area of 26.4 km<sup>2</sup>. The median glacier elevation is 6,025 m a.s.l. from the terminus at 4,879 m a.s.l. to the headwall at 7,981 m a.s.l. (RGI 7.0 Consortium, 2023). The stagnant debris-covered tongue has an area of 6.2 km<sup>2</sup> (23% of the total glacier). The ‘Little Ice Age’ (LIA) maximum of Khumbu Glacier occurred about 200–500 years before present, which is consistent with ages produced for moraines elsewhere in the central Himalaya (Hornsey et al., 2022; Rowan, 2017). Khumbu Glacier was slightly larger than today during the late Holocene, transitioning from a clean-ice glacier with high velocities and efficient export of debris to a debris-covered glacier with lower velocities after the LIA; this change was initiated by the reduction in ice flux to the glacier tongue promoted by a rise in ELA (Rowan et al., 2015). Observations and modelling of the dynamics and structure of Khumbu Glacier show that the tongue for 5 km upglacier from the terminus (25% of the total length, 20% of total ice volume) is stagnant and dynamically detached from the active glacier in the last century (Miles et al., 2022; Quincey et al., 2009; Rowan et al., 2021). Basal ice at the glacier surface indicates that the active terminus overrides the stagnant glacier tongue (Miles et al., 2021) and measurements of surface displacement show no longitudinal flow through the detached debris-covered tongue, which is collapsing laterally at a rate of about  $3 \text{ m a}^{-1}$  (Watson et al., 2017).<sup>4</sup>

**Deleted:** an

**Formatted:** Superscript

**Formatted:** Superscript

213 and ablation was calculated as a function of elevation  $0.5 \text{ m m}^{-1}$  up to a maximum of  $2.0 \text{ m w.e. a}^{-1}$ .  
214 This simulation continued through the LIA forced by a step change in mean annual air temperature  
215 (MAAT) equivalent to  $1.5^\circ\text{C}$  colder than the present day over 500 years following the approach of  
216 Rowan et al. (2015, 2021). Ice-marginal moraines denoting the late Holocene ( $1.3 \pm 0.1 \text{ ka}$ ) glacier  
217 extent and thickness (Hornøy et al., 2022) were used to constrain the spin-up simulation.

Formatted: Not Superscript/ Subscript

218  
219 The late Holocene simulation was forced to present-day (2015 CE) conditions using three surface mass  
220 balances (one from each RCM) calculated using the Coupled Snowpack and Ice-surface Energy and  
221 Mass Balance model in Python (COSIPY v1.3) (Sauter et al., 2020). These simulations were evaluated  
222 against a range of observations of present-day glaciology and previous glacier model experiments (Fig.  
223 3), and the experiment using the NOAA RCM was identified as the starting point for all future  
224 simulations because this was most representative of the observed glacier. We simulated only the active  
225 section of the glacier beyond 2015 CE and added the dynamically detached debris-covered tongue  
226 simulated at the present day to the model domain as a static topographic feature for the future  
227 simulations. The volume of the detached tongue was calculated by using the simulated present-day  
228 velocity field to separate the simulated present-day ice volume where velocities declined below  $10 \text{ m}$   
229  $\text{a}^{-1}$ . Thus, we arrived at the present-day from the LIA maximum simulation by forcing the LIA glacier  
230 with the 2015–2020 CE mass balance.

Deleted: assigned

Deleted: by using

Formatted: Superscript

Deleted: for 200 years

231  
232 We used the output from the present-day simulation with the 2095–2100 CE mass balance calculated  
233 using COSIPY to force the model to 2100 CE. The glacier model simulations continued from the present  
234 day to 2100 CE forced by distributed glacier surface mass balances calculated for each of the three  
235 RCMs and two RCPs using COSIPY. The three RCMs and two future RCPs represented a range of  
236 possible future climates with distinctly different precipitation trends—equivalent to dry, moderate, and  
237 wet scenarios for warming of  $1.4\text{--}2.2^\circ\text{C}$  under RCP4.5 and  $3.8\text{--}4.1^\circ\text{C}$  under RCP8.5 (Table 1; Fig. 2D;  
238 Section 2.3). We used time slices representing the present day (2015–2020 CE) and the end of the 21<sup>st</sup>  
239 Century (2095–2100 CE) to calculate surface mass balance, and the preceding decade was used to  
240 evaluate these time slices (see Section 3.3). We used this step forcing, whereby the future mass balance  
241 was imposed and the glacier adjusted to this from the start of the century in question, rather than  
242 interpolating mass balance over time to reduce the computational expense of the surface mass balance  
243 and glacier modelling (~24 hours per simulation).

Deleted: for a period of 80 years

244  
245 Estimates from a global glacier modelling study indicate that avalanching contributes up to 18% of  
246 regional accumulation to glaciers in the monsoon-influenced Himalaya (Kneib et al., 2025) and  
247 observations of high-elevation Himalayan glaciers, including Khumbu Glacier, suggest that up to 75%  
248 of accumulation occurs by avalanching rather than direct snowfall (Fig. 1D) (Benn and Lehmkühl,  
249 2000; Laha et al., 2017). Avalanching affects mountain glaciers in two ways; (1) by moving snow from  
250 steep hillslopes onto the glacier surface thus increasing accumulation from that calculated from direct  
251 snowfall onto the glacier surface, and (2) by redistributing snow across steep sections of the glacier  
252 surface (Kneib et al., 2025). We examined the uncertainty in accumulation resulting from the application  
253 of a calculation in iSOSIA to move snowfall from slopes susceptible to avalanching (see Section 2.6).  
254 If avalanching was not considered in iSOSIA, then the accumulation of snow calculated using COSIPY  
255 within the catchment but outside of the glacier outline would have no impact on accumulation resulting  
256 in an underestimation of ice volume, and the steep sections of the glacier would hold more mass than  
257 expected. For example, when avalanching was not simulated and accumulation occurred at a uniform  
258 rate of  $2.0 \text{ w.e. m a}^{-1}$  across the Western Cwm accumulation area, Khumbu Glacier had a similar extent  
259 but a volume more than double that of the glacier simulated with avalanche redistribution of snow,  
260 because mass was not redistributed effectively across steep sections of the glacier surface (result not  
261 shown).

Moved down [2]: We tested a range of lapse rates from  $-3.0^\circ\text{C km}^{-1}$  to  $-6.0^\circ\text{C km}^{-1}$  while maintaining the same ELA based on the range of monthly values calculated from regression of NASA MODIS land surface temperature data for the Central Himalaya, which resulted in a difference in ice volume of  $0.4 \times 10^9 \text{ m}^3$  and no change in glacier length at the present day (result not shown).

## 262 2.2 Meteorological data collection and analysis

263  
264 The first meteorological observations for the Nepal Himalaya were collected during the 1970s and  
265 found a trend of diurnal precipitation on ridges and nocturnal precipitation in valley floors (Ageta, 1976)  
266 reflecting cloud development from orographic convection during the day. Continuously recording AWS  
267 were first installed in the region in the 1990s at the Pyramid Observatory near Lobuche village, where

279 Bollasina et al. (2002) analysed of the monsoon from meteorological observations collected between  
280 1994 and 1999, finding that the onset (decay) of the Indian Summer Monsoon was distinguished by  
281 higher (lower) daily precipitation totals, mean relative humidity and atmospheric pressure and a reduced  
282 (increased) diurnal range in atmospheric temperature. Bollasina et al. (2002) identified two daily  
283 profiles in precipitation and wind direction thought to be related to the monsoon. In addition, five-day  
284 and ten-day precipitation cycles were observed linked to oscillations in the Tibetan High. A new AWS  
285 was installed at the Pyramid Observatory at 5,035 m a.s.l. in September 2000 as part of a network in  
286 the Dudh Koshi valley of six AWS between 2,680 to 5,700 m a.s.l., in addition to some short-lived  
287 higher-elevation stations, maintained by the Ev-K2-CNR network. The Pyramid Observatory AWS  
288 included a snow depth sensor between 2009 and 2010, but the data were discontinuous and inconsistent,  
289 and the measurement period ended in December 2010. A second AWS was installed in the same location  
290 by the GlacioClim network in 2013 (Wagnon et al., 2013; Sherpa et al., 2017) provides a longer period  
291 of continuous data collection. More recently, a network of 5 AWS including the highest elevations in  
292 the Khumbu catchment were installed by the National Geographic project at Phortse (3,810 m a.s.l.),  
293 Everest Base Camp (5,315 m a.s.l.), Camp 2 (6,464 m a.s.l.), the South Col (7,945 m a.s.l.) and the  
294 Balcony (8,430 m a.s.l.) (Matthews et al., 2020). However, at time of writing, there are no continuous  
295 records of high-elevation meteorological variables that span a longer period than 15 years, making the  
296 calculation of climate normals impossible. In this study, we analysed data from these various sources  
297 for evaluation of mesoscale trends in the upper Khumbu Valley and for use to downscale RCMs and  
298 evaluate the results of our calculations. The location of the AWS is shown in Fig. 1C. Gaps in the air  
299 temperature and precipitation data were filled using interpolated data from neighbouring stations where  
300 required (as described in Appendix A).

301  
302 The AWS data were used to make a reference simulation in COSIPY of the surface energy fluxes and  
303 mass balance of the Khumbu Glacier catchment between 2013–2015 for model development and  
304 sensitivity experiments (Fig. 4 and Fig. 5). We compiled 14 years of meteorological observations from  
305 the two AWS provided by the GlacioClim network at the Pyramid Observatory (5,050 m a.s.l. and 5,035  
306 m a.s.l.) and the West Changri Nup Glacier AWS (5,363 m a.s.l.) (Wagnon et al., 2013; Sherpa et al.,  
307 2017). All meteorological data were collected for the period December 2010 to November 2019, apart  
308 from precipitation which was only recorded between December 2012 to November 2016. All  
309 meteorological data (excluding precipitation) used for the reference simulation were taken from the  
310 West Changri Nup AWS. Given the frequency of missing precipitation data from the AWS, the  
311 undercatch of snow associated with tipping bucket rain gauges, and the scarcity of high-elevation  
312 precipitation measurements, precipitation was not varied with elevation in the reference simulation.  
313 Precipitation data for the reference simulation were collected from the GlacioClim Geonor precipitation  
314 gauge at the Pyramid Observatory (5,035 m a.s.l.) because this precipitation gauge provides a longer  
315 period of continuous observations than the other gauges and avoids errors due to low precipitation  
316 amounts measured by tipping bucket gauges, which are known to systematically underestimate snowfall  
317 particularly during high winds (Sherpa et al., 2017). Precipitation was measured at 15-minute intervals  
318 using a Geonor T-200BM sensor mounted 1.8 m above the surface. Evaporation from the bucket was  
319 blocked by a layer of oil, but some loss did occur, as evidenced by precipitation values below 0 mm.  
320 Noise from wind and evaporation were corrected for by compensating any negative change over the  
321 15-minute time step with the neighbouring positive value such that accumulated precipitation was  
322 unchanged. Periods with prolonged evaporation were set to zero. Undercatch of snowfall by rainfall  
323 gauges was corrected through precipitation phase partitioning using wind speed observations (Wagnon  
324 et al., 2009). Air temperature was interpolated to match the height of the precipitation gauge using  
325 hourly lapse rates that averaged  $-5.89\text{ }^{\circ}\text{C km}^{-1}$ . COSIPY was run for both elevations using the non-  
326 adjusted temperature data for 5,336 m a.s.l. and the adjusted temperature data for 5,035 m a.s.l. and it  
327 made little impact on the model results. Simulated meteorological variables were evaluated at the  
328 highest elevations using the National Geographic AWS stations at Camp 2 (6,464 m a.s.l.) and the South  
329 Col (7,945 m a.s.l.) using data for May–November 2019 (Matthews et al., 2020).

330  
331 Direct solar radiation across the model domain was corrected for the slope, azimuth, and shadowing  
332 potential of each pixel (Wohlfahrt et al., 2016; Sauter et al., 2020). A footprint-weighted correction was  
333 also applied to horizontal measurements of net radiation. The fraction of diffuse incoming shortwave

334 radiation was estimated by using the ratio of total shortwave (global) radiation and potential shortwave  
335 radiation to define a clearness index (Wohlfahrt et al., 2016). This clearness index was used to calculate  
336 diffuse radiation, which was calibrated with data from the Neustift eddy covariance station in the  
337 Austrian Alps (Wohlfahrt et al., 2008). Pressure was distributed across the domain by first calculating  
338 sea-level pressure (*cf.* Lente and Osz, 2020) and then interpolated with the barometric equation. The  
339 relative humidity gradient was calculated as  $-0.002\% \text{ m}^{-1}$  using data from the Ev-K2-CNR and the  
340 GlacioClim AWS networks, and evaluated by comparison with measurements made by the National  
341 Geographic network AWS ranging in elevation from 3,810–8,430 m a.s.l. (Matthews et al., 2020) to  
342 capture trends at higher elevations. The distributed radiative fluxes were compared with the same high-  
343 elevation stations for 2019 to assess the efficacy of this method across the domain. Wind speed was  
344 assumed to be uniform across the domain.

### 345 **2.3 Present-day RCM downscaling using meteorological observations**

346 Six RCMs were assessed on their fidelity to present-day climate using hindcasting (Biemans et al.,  
347 2013) with an emphasis on temperature seasonality and seasonal precipitation dynamics given the  
348 importance of these variables for glacier mass balance. RCMs from the Coordinated Regional  
349 Downscaling Experiment (CORDEX) South Asia domain were dynamically downscaled from CMIP5  
350 GCMs by the Indian Institute of Tropical Meteorology to a 50 km spatial resolution (Lutz et al., 2016)  
351 and collected for the grid box containing Khumbu Glacier (27.9065056°N, 86.4352951°E). Three of  
352 the six CORDEX South Asia RCMs (NOAA, CCCma, IPSL) spanning a range of possible future  
353 precipitation conditions (Table 1) were selected as discrete scenarios for the glacier surface energy and  
354 mass balance calculations. The three remaining RCMs were discounted due to being intermediate to  
355 those selected for our experiments (i.e. close to the future precipitation scenario represented by CCCma)  
356 or particularly poor at reproducing seasonal temperature and precipitation cycles. For example, despite  
357 the annual precipitation sums from the CSIRO RCM being closest to observed values and having the  
358 potential to be the ‘driest’ scenario examined, analysis of precipitation seasonality indicated that the  
359 monsoon signal was completely absent with this RCM instead showing a strong dominance of winter  
360 precipitation.

361  
362 The present-day RCM results were downscaled using quantile mapping, also known as “distribution  
363 mapping”, using 14 years of observations collected between January 2006 and November 2019 from  
364 three AWS as described in Section 2.2. Parametric quantile mapping (Piani et al., 2010) was used to  
365 downscale the RCM to a daily time step at the resolution of the DEM, whereby a statistical relationship  
366 between the raw climate model outputs and observations was formed by substituting the RCM results  
367 with observations at a cumulative density function of the prescribed distribution (e.g., a Gaussian  
368 distribution for temperature; Luo et al., 2018; a gamma distribution for precipitation; Piani et al., 2010).  
369 This correction was applied to the raw RCM outputs to produce a third downscaled dataset which had  
370 an improved fit to the observations (Fig. 2C and 2D). The quantile mapping approach was chosen  
371 because this is effective for downscaling precipitation and reduces errors in the standard deviation, the  
372 coefficient of variation, and the skewness of distributed values relative to other methods (Lafon et al.,  
373 2013; Reiter et al., 2018). The AWS data were used to disaggregate the daily downscaled present-day  
374 and end-of-century climate model outputs to an hourly resolution for energy balance modelling. All  
375 meteorological variables, excluding precipitation, were downscaled using the MELODIST Python tool  
376 (Förster et al., 2016). Seasonal means were applied for precipitation to reproduce the ‘nocturnal peak’  
377 seen during the monsoon that MELODIST was unable to replicate (Figs. A1, A2 and A3). Further  
378 information on the meteorological data analysis and RCM downscaling are provided in Appendix A.

### 379 **2.4 Future RCM downscaling**

380  
381 Two future emission scenarios (RCP4.5 and RCP8.5) were available from CORDEX South Asia, which  
382 represent intermediate and high emissions by 2100 CE relative to the present day. These two emissions  
383 scenarios are frequently used in climate impact studies enabling the comparison of our results with  
384 studies that use other climate/glacier model projections. The two future emissions scenarios were  
385 analysed for each of the three CORDEX RCMs to account for the inherently high uncertainties in future  
386 precipitation trends associated with climate models and the interplay of changing precipitation with  
387 atmospheric warming. The same statistical downscaling approach and disaggregation used for the three  
388

389 present-day RCMs described in Section 2.3 was applied to the raw CORDEX RCM daily outputs for  
390 the three future RCM time slices under RCP4.5 and RCP8.5. The temperature change between the  
391 present day and the future time slices was preserved and there was no evidence of any imposed  
392 strengthening in the monsoon resulting from downscaling. An increase in the frequency of days per  
393 year outside of the monsoon season with high precipitation amounts (defined here as over 15 mm of  
394 daily precipitation) accounted in large part for the higher annual precipitation amounts relative to the  
395 present day that were found in four out of the six RCMs. However, the total future annual precipitation  
396 increase was on average 8.8% greater in the downscaled climates relative to the raw RCMs, suggesting  
397 that this positive trend was inflated by downscaling. The downscaled climates reduced the frequency  
398 of precipitation, although, as in present day observations, monsoon precipitation occurred frequently  
399 and could be characterised as predominantly drizzle in the future.

## 400 2.5 Surface energy balance modelling

401 COSIPY is a leading open-source method for estimating glacier surface mass balance and has  
402 previously been applied to glaciers in High Mountain Asia. COSIPY includes a calculation of  
403 sublimation, which is an important ablation process for high-elevation glaciers because ablation can  
404 still occur if the latent heat flux is negative through sublimation, even in instances where surface  
405 temperature and/or air temperature are well below the melting point (Bonekamp et al., 2021; Brun et  
406 al., 2023; Huintjes et al., 2015). COSIPY resolves all energy fluxes ( $F$ ) at the ice surface that contribute  
407 to surface melt ( $Q_{melt}$ ):

$$408 F = SWin \cdot (1-\alpha) + LWin + LWout + Qsens + Qlat + Qg + Qliq \quad \text{Eq. (1)}$$

409  
410 Where  $SWin$  is incoming shortwave radiation,  $\alpha$  is albedo,  $LWin$  and  $LWout$  are incoming and outgoing  
411 longwave radiation, and  $Qsens$ ,  $Qlat$ , and  $Qg$  are the sensible, latent, and ground heat fluxes (Oerlemans  
412 et al., 2001) and  $Qliq$  is the heat flux from liquid precipitation; the latter variable is often neglected in  
413 ablation calculations (Cuffey and Paterson, 2010) but is of particular importance here as the Indian  
414 Summer Monsoon brings a significant amount of liquid precipitation to the lower reaches of Khumbu  
415 Glacier. The resulting  $F$  is equal to the energy available for surface melt ( $Q_{melt}$ ) when surface  
416 temperature ( $T_s$ ) is at melting point ( $0^\circ\text{C}$ ).  $T_s$  is used to calculate  $LWout$ ,  $Qsens$ ,  $Qlat$ ,  $Qg$  and to partition  
417 solid and liquid precipitation. When  $T_s$  exceeds the melting point it is reset to  $0^\circ\text{C}$  (273.15 K) and the  
418 residual  $F$  fluxes equal  $Q_{melt}$ . In this instance, subsurface melt is triggered when the energy fluxes, for  
419 example, penetrating  $SWin$  warm the ice layer so that  $T_s$  exceeds the melting point of ice (Sauter et al.,  
420 2020).

421  
422 The COSIPY model domain was taken from the 30-m DEM that was resampled to 200-m grid spacing  
423 following a reference simulation for 2013–2015 and sensitivity analyses, which revealed minimal  
424 impact on the results whilst greatly reducing computational expense (Fig. 4). The sensitivity of glacier  
425 mass balance to individual meteorological variables (MAAT, radiative fluxes, relative humidity, lapse  
426 rate, precipitation amount, precipitation phase, glacier surface roughness) was calculated in sensitivity  
427 experiments using the reference simulation that perturbed these variables individually. Perturbations  
428 were made within the range of the possible uncertainties for each variable that arise from a combination  
429 of the choice of observations or climate models, the downscaling approach used, and the distribution of  
430 meteorological variables (see Section 3.1). The values used for perturbations of MAAT and  
431 precipitation amount were similar to those expected for possible future climate forcings. We tested a  
432 range of lapse rates from  $-3.0^\circ\text{C km}^{-1}$  to  $-6.0^\circ\text{C km}^{-1}$  while maintaining the same ELA based on the  
433 range of monthly values calculated from regression of NASA MODIS land surface temperature data for  
434 the Central Himalaya, which resulted in a difference in ice volume of  $0.4 \times 10^9 \text{ m}^3$  and no change in  
435 glacier length at the present day (result not shown).

436  
437 The downscaled and disaggregated CORDEX RCM daily climate variables (temperature, precipitation,  
438 the radiation components, wind speed, relative humidity and atmospheric pressure) were used to force  
439 COSIPY for the periods 2015–2020 CE and 2095–2100 CE. While snowfall measurements can be used  
440 as an input to COSIPY, there are no good-quality measurements of snowfall in the Everest region and  
441 so precipitation was partitioned into rainfall and snowfall using the snow transfer scheme within

Deleted: and

Moved (insertion) [2]

445 COSIPY (Sauter et al., 2020). COSIPY was forced using hourly meteorology with nine variables to  
446 calculate the energy balance and mass balance components at an hourly time step from the sum of  
447 accumulation by solid precipitation, deposition, and refreezing of melt water percolation, and ablation  
448 by melt and sublimation. The exchange processes at the surface, including energy release and  
449 consumption with phase changes, control temperature distribution and phase changes within the glacier  
450 (comprised of horizontal ice and snow layers), and accounts for meltwater refreeze and percolation with  
451 the meltwater produced from the surface melt calculations acting as an input. The impacts of  
452 supraglacial debris on ablation and of snow avalanching on accumulation were handled in iSOSIA, as  
453 described in the next section.

## 454 455 2.6 Ice-dynamical glacier evolution modelling

456 The second-order shallow ice approximation model (iSOSIA) is a 3-D higher-order ice-dynamical  
457 glacier evolution model that solves for the flow of ice including longitudinal and transverse stress  
458 gradients that are imposed on ice flow through high-relief topography (Egholm et al., 2011). This glacier  
459 model simulates the evolution of debris-covered glaciers by incorporating the feedbacks between debris  
460 transport, mass balance and ice flow (Rowan et al., 2015) and includes two processes that are important  
461 for many Himalayan glaciers; (1) the redistribution of snow by avalanching that is estimated to account  
462 for up to 75% of accumulation, and (2) the formation and evolution of a supraglacial debris layer that  
463 insulates the ice surface to modify ablation (Rowan et al., 2015). While previous versions of this glacier  
464 model used depth-integrated ice flow, this version simulates ice flow through Khumbu Glacier in 3-D  
465 as the ice thickness is divided into 20 vertical layers to calculate englacial debris transport (Rowan et  
466 al., 2015). The glacier model has a variable time step that can adjust up to a maximum of 0.1 years to  
467 allow greater computational efficiency.

468  
469 The distributed surface mass balances calculated using COSIPY using the downscaled RCMs for the  
470 periods 2015–2020 CE and 2095–2100 CE were used as inputs to the glacier model with no change in  
471 forcing applied between these two periods. The model domain topography was the same in iSOSIA as  
472 that used in COSIPY. Surface processes within the glacier model modified the distribution of  
473 accumulation and ablation but this was not updated into the surface topography used in COSIPY.  
474 Simulated accumulation was the result of the total snowfall in each cell and avalanching of snow  
475 imposed for the accumulated snowpack from hillslopes by removing snow and ice from hillslopes  
476 greater than 28° and redistributing this mass across less steep surfaces using a non-linear hillslope flux  
477 model (Roering et al., 1999). The avalanching routine was found to be sufficient to prevent snow and  
478 ice accumulation on slopes that are observed to be free of glacier ice such as the southwest face of  
479 Sagarmatha (Mt. Everest) while allowing accumulation on steep sections of the glacier (Rowan et al.,  
480 2015) resulting in accumulation rates at the glacier surface in line with the limited available  
481 observations for Himalayan glaciers of 2 m water equivalent (w.e.) per year (Benn and Lehmkuhl,  
482 2000).

483  
484 Rock avalanching is responsible for much of the debris accumulation on the glacier surface but there is  
485 little information about the magnitude and frequency of these events, so headwall erosion was assumed  
486 to be uniform at  $1 \text{ mm a}^{-1}$  (Rowan et al., 2021). Debris produced by headwall erosion was delivered to  
487 the glacier surface using a similar non-linear hillslope flux model to snow avalanching. The reduction  
488 in ablation beneath supraglacial debris from clean-ice values was represented as a reciprocal function  
489 that scaled clean-ice ablation ( $b_{clean}$ ) to give sub-debris melt ( $b_{debris}$ ) as a function of debris thickness  
490 ( $h$ ):

491  
492 
$$b_{debris} = b_{clean} \times \frac{h_0}{h + h_0} \quad \text{Eq. (2)}$$

493  
494 where  $h_0$  is a constant representing the characteristic debris thickness at which the reduction in ablation  
495 due to insulation by supraglacial debris is 50% of the value for an equivalent clean-ice surface  
496 (Anderson and Anderson, 2016; Rowan et al., 2021). The observed heterogeneity of surface ablation  
497 required a parameterisation of sub-debris melt representing the effects of differential ablation, which  
498 was represented in Equation (2) using a value for  $h_0$  of 0.8 m (Bartlett et al., 2021; Rowan et al., 2021;

Deleted: time steps

500 Strickland et al., 2023). We note that Equation (2) represents an empirical calculation of the impact of  
501 supraglacial debris on glacier surface melt that is calibrated to observations of sub-debris melt rates for  
502 glaciers in the Central Himalaya (Rowan et al., 2021) and as such, changes in surface energy balance  
503 processes including vapour fluxes within the debris-covered section of the glacier are not included.  
504

### 505 3. Results

#### 506 3.1 COSIPY parameter perturbations

507 The spatially averaged mass balance was most sensitive to changes in MAAT (perturbed by  $\pm 1.5^\circ\text{C}$ ,  
508  $2.0^\circ\text{C}$  and  $3.0^\circ\text{C}$ ),  $LWin$  and  $SWin$  ( $\pm 10\%$  and  $20\%$ ). Perturbations of relative humidity ( $\pm 10\%$  and  
509  $\pm 20\%$ ) had the least impact on mass balance. The use of a seasonal lapse rate of  $5.38^\circ\text{C km}^{-1}$  yielded a  
510 spatially averaged mass balance that was 5.6% less than the reference calculation value, while a diurnal  
511 lapse rate gave a mass balance that was only 0.45% lower because the reference lapse rate was close to  
512 the mean of the day/night lapse rates, whereas the environmental lapse rate ( $6.50^\circ\text{C km}^{-1}$ ) gave a mass  
513 balance that was 1.24% higher than the reference value. The relatively small difference in mass balance  
514 due to the choice of lapse rate is due to the extremely high elevation of Khumbu Glacier, which means  
515 that MAAT is below  $0^\circ\text{C}$  in the accumulation area for much of the year and a higher lapse rate does not  
516 affect rain/snow partitioning. The largest difference in mass balance due to the choice of lapse rate  
517 occurred just below the ELA and resulted in a difference of  $\pm 24\%$  in spatially averaged mass balance  
518 for this section of the glacier. The National Geographic AWS on Mt. Everest provided an opportunity  
519 to examine lapse rates at the highest elevations. For the period April–November 2019, the observed  
520 lapse rate was  $4.68^\circ\text{C km}^{-1}$  between Phortse (3,810 m a.s.l.) and Everest Base Camp (5,315 m a.s.l.),  
521 and  $5.36^\circ\text{C km}^{-1}$  between Camp II and South Col, similar to the value used in this study. The lapse rate  
522 above 8,000 m a.s.l. was about  $1.2^\circ\text{C km}^{-1}$  greater than that below 5,600 m a.s.l. between the two highest  
523 AWS at the South Col (7,945 m a.s.l.) and the Balcony (8,430 m a.s.l.) indicating that in the highest-  
524 elevation sections of the catchment, lapse rates may be best represented by values considered suitable  
525 for the free atmosphere.  
526

527 Coupled parameter testing was carried out to perturb precipitation and MAAT simultaneously. The most  
528 significant change in spatially averaged mass balance followed a  $3^\circ\text{C}$  increase in MAAT and 20%  
529 decrease in precipitation amount. The change in ablation following an increase in temperature of  $1.5^\circ\text{C}$   
530 was compensated by accumulation resulting from 20% higher precipitation. The impact on mass  
531 balance of two precipitation phase (rain/snow) partitioning schemes was investigated and compared  
532 with the default snow transfer function in COSIPY; (1) using threshold temperatures of  $0.5^\circ\text{C}$ ,  $2.0^\circ\text{C}$ ,  
533 and  $3.5^\circ\text{C}$ , and (2) using a calculation that smoothly scaled rain/snow partitioning from 100% solid  
534 precipitation at  $-1^\circ\text{C}$  to 0% solid precipitation at  $4^\circ\text{C}$ . The height of the  $0^\circ\text{C}$  isotherm during months  
535 that experienced significant ablation (May–September) fluctuated around 5,125–6,250 m a.s.l., which  
536 correlated with the elevations that experienced the greatest mass balance change with lapse rate. While  
537 the lapse rate used to distribute MAAT did not have a significant impact on glacier-wide mass balance,  
538 the elevation of the  $0^\circ\text{C}$  isotherm from the pre-monsoon until the end of the monsoon was sensitive to  
539 the air temperature distribution.  
540

541 The glacier ice surface roughness ( $z_0$ ) value was 1.7 mm (Table 2), which is a reasonable estimate for  
542 clean-ice glaciers (Mölg et al., 2012). The  $z_0$  values reported in the literature vary widely, even for clean-  
543 ice glaciers, and do not consider debris-covered glacier surfaces, and so two substantially different  $z_0$   
544 values were tested as end-members of the likely range in  $z_0$  values for Khumbu Glacier. Values for  $z_0$  of  
545 0.1 mm from Midtre Lovénbreen in Svalbard (Irvine-Fynn et al., 2014) and August-One Glacier in  
546 China (Guo et al., 2018), and a value of 6.9 mm for the clean-ice section of Haut Glacier D’Arolla  
547 (Brock et al., 2006) were all tested in the reference simulation. Adjusting  $z_0$  had minimal impact on  
548 mass balance, although a higher (lower)  $z_0$  did result in slightly increased (decreased) mass balance.  
549  
550

#### 551 3.2 Evaluation of the COSIPY surface energy balance model results

552 The reference simulation represented the period 2013–2015 CE and was forced with AWS data using  
553 the model parameters in Table 2. Turbulent fluxes and energy balance components across Khumbu  
554 Glacier were explored across the 2013–2015 reference period to assess the performance of COSIPY

555 and understand their relative spatial importance (Fig. 5). The glacier-wide clean-ice mass balance for  
556 the three-year reference period was  $-3.4$  m w.e., which equates to  $-1.13$  m w.e  $a^{-1}$ . Maximum ablation  
557 was up to  $16.2$  m w.e. over three years (Fig. 4). High precipitation events were observed to offset some  
558 ablation if they occurred outside the core monsoon season (e.g., in October 2013 and May 2014) but  
559 did not influence monsoon season ablation when high air temperatures and strong incoming radiative  
560 fluxes rapidly remove snow cover and drive melting. Higher minimum temperatures in winter 2013–  
561 2014 CE relative to the other winters did not significantly influence accumulation rates, which remained  
562 similar to those in 2014–2015 CE. Low precipitation amounts during the 2015 monsoon (286 mm in  
563 2015, compared to 330.8 mm in 2013, and 333.9 mm in 2014) resulted in lower accumulation in the  
564 upper reaches of the glacier. The precipitation gradient was calibrated to  $1 \times 10^{-5} \% m^{-1}$  to match  
565 observed accumulation rates. However, this gradient largely arises from avalanching (Benn and  
566 Lehmkühl, 2000) which is challenging to represent in COSIPY and was instead handled in the glacier  
567 model (Section 2.6).

568  
569 The energy available for ablation peaked in the pre-monsoon and monsoon, bringing higher rates of  
570 sublimation and subsurface melt in April–June (Fig. 5). Simulated sublimation occurred at all  
571 elevations, with the highest cumulative loss near the South Col (EB7910) where sublimation dominated  
572 mass balance and only slightly slowed from December until May. Sublimation rates were increasingly  
573 tied to seasonality with distance down-glacier, with rates on the lower section of the tongue (EB4980)  
574 increasing from April until the start of the monsoon in July. Calculated subsurface melt was negligible  
575 at or above the ELA (5,950 m a.s.l.) whereas at lower elevations sub-surface melt dominated mass  
576 balance with a stronger seasonal cycle related to surface temperature. The interannual variability in  
577 subsurface melt was linked to surface temperature, although low simulated subsurface melt rates in the  
578 first year of the reference simulation were largely due to persistence of the initial snow cover that  
579 shielded the subsurface from relatively warm air temperatures until the subsurface adapted to local  
580 conditions. Refreezing occurred across the entire glacier, with a staggered onset due to increased  
581 elevation, and the absolute values were low (Fig. 5). The higher latent heat flux during the monsoon  
582 resulted in higher deposition of snow to the glacier at the lower elevations, with negligible rates at  
583 higher elevation. Similar absolute values and patterns are seen for condensation.

584  
585 Calculated incoming shortwave radiation matched well with AWS observations, indicating that the  
586 radiation model in COSIPY performed well across the extreme relief of the Khumbu Glacier catchment.  
587 Net shortwave radiation contributed the largest energy input to the glacier surface at lower elevations,  
588 correlating most strongly with the energy available for melt, with a mean correlation coefficient of 0.79.  
589 There was high temporal variability related to variable cloud cover exhibited in the hourly incoming  
590 shortwave radiation forcing and fluctuating albedo during the warmer months with the melting of the  
591 snowpack. The high incoming shortwave radiation the upper reaches of the glacier indicate that low net  
592 shortwave radiation is not due to topographic shading. Net shortwave radiation was correlated with  
593 albedo ( $r = 0.86$ ), and the persistence of snow throughout much of the year reduced the energy available  
594 for melt. Net longwave radiation also contributed to the energy available for melt as the pattern of both  
595 fluxes corresponded. Between 5,900–7,900 m a.s.l., net longwave radiation sometimes exceeded zero  
596 during the monsoon, most likely due to heavy cloud cover and increased temperatures relative to the  
597 glacier surface. The latent heat flux was almost zero at the lower elevation sites as the arrival of the  
598 monsoon resulted in higher relative humidity, and this pattern was similar, but dampened, at higher  
599 elevation. At the South Col (EB7910) the energy available for melt correlated most closely with the  
600 sensible heat flux (Fig. 5).

Deleted: exactly ( $r = 1$ )

601  
602 Grid spacings for the model domain of 30 m, 50 m, 200 m and 1 km were tested to ensure that that the  
603 COSIPY calculations captured orographic effects without unnecessary computational expense (Fig. 4).  
604 The simulated maximum accumulation rate did not change significantly with grid spacing, giving  
605 accumulation rates of 2.1–3.9 m w.e. at 6,500–7,000 m a.s.l. in the reference simulation. The 1 km grid  
606 spacing contained only 27 glacier points, and gave a similar spatial mean mass balance to the finer-  
607 resolution calculations, but there were large gaps in mass balance calculated across the glacier that  
608 affected the height of the ELA and significantly reduced the calculated maximum accumulation value.  
609 The 30-m and 50-m grid spacings captured greater spatial variability in mass balance relative to the 200

611 m resolution calculation, particularly at elevations between 5200–5400 m a.s.l. (Fig. 4). However, as  
612 the ELA, and the calculated maximum and minimum mass balances were not significantly different  
613 between these finer-resolution calculations, the 200 m grid spacing was used throughout to benefit from  
614 the much reduced computational expense.

### 616 3.3 Evaluation of the RCM downscaling

617 The downscaled climate variables from the three RCMs for the present-day time slices (2015–2020 CE)  
618 were evaluated against 14 years of observations from three AWS to assess the representation of means,  
619 seasonality, diurnal cycles, day-to-day variability, and interannual variability (Fig. 2C and 2D). All three  
620 downscaled RCMs showed good agreement between MAAT ( $-2.15 \pm 0.05^\circ\text{C}$ ) and observed air  
621 temperature from the Pyramid AWS (Figs. A1 and A2). The representation of the monsoon was greatly  
622 improved by the RCM downscaling; temperature seasonality was well resolved following quantile  
623 mapping and the monthly mean and minimum air temperatures were similar to observations across the  
624 present-day time slice (Fig. A1). The monsoon stabilised air temperatures and reduced the range  
625 between minimum and maximum temperatures in the downscaled RCMs, which was in better  
626 agreement with AWS observations, but was not present in the raw RCMs prior to downscaling. We note  
627 that the downscaled maximum air temperature was at times higher than observations amongst all RCMs  
628 during the post-monsoon and winter (Fig. A1) but the distribution of downscaled air temperatures was  
629 similar to observed values (Fig. A2). Gamma-distribution quantile mapping substantially improved the  
630 absolute precipitation values relative to the AWS observations compared to those in the raw RCMs; the  
631 overestimation of winter precipitation and relative underestimation of monsoon precipitation amounts  
632 in the raw RCMs was reduced and downscaled results show a clearer monsoon signal (Fig. A3). When  
633 compared with AWS observations, RCM downscaling slightly overcorrected the seasonal precipitation  
634 pattern with a slight underestimation of winter precipitation for the most extreme winter events. Across  
635 the three present-day RCM simulations, the surface mass balance calculated using the NOAA RCM  
636 was more positive than that for the ISPL and CCCma RCMs and most similar to the mass balance  
637 calculated from meteorological observations, and remained the most positive mass balance in the end-  
638 of-century time slices (Fig. 6).

### 640 3.4 Evaluation of the iSOSIA glacier evolution model results

641 COSIPY was used to calculate clean-ice surface mass balance from the downscaled RCMs, and the  
642 insulating effects of supraglacial debris were calculated in iSOSIA. The simulated glacier geometry and  
643 dynamics were compared with remotely sensed observations of ice thickness, supraglacial debris  
644 distribution, velocity, and surface elevation change for the present-day glacier (Fig. 3) and varied  
645 depending on the RCM used as forcing (Fig. 7). The experiment using the NOAA RCM was identified  
646 as the starting point for all future simulations because this was most representative of the observed  
647 glacier at 2015 CE (Fig. 3). The distributed surface mass balances calculated using COSIPY were most  
648 similar to observed values after the calculated surface mass balances were integrated with the glacier  
649 model to include accumulation by snow avalanching and the reduction in surface melting beneath  
650 supraglacial debris; the active glacier extent was underestimated if supraglacial debris is not simulated  
651 (Fig. 8). The supraglacial debris-mass balance feedback in the glacier model reproduced the observed  
652 reversed mass balance gradient and peak in ablation below the Khumbu Icefall (Fig. 1D).

654 The simulated glacier area was  $7.8 \text{ km}^2$  and similar to that obtained from structural mapping in 1979  
655 CE (Nakawo, 1986). Radio-echo sounding in 1999 CE obtained ice thickness estimates close to the  
656 active terminus of  $\sim 160 \text{ m}$  (Gades et al., 2000) and simulated ice thickness at the terminus was  $130 \text{ m}$   
657 (Fig. 3A). The simulated thickness at the active glacier terminus thickness was approximately  $175 \text{ m}$  in  
658 1999 CE, which agreed well with observations from DEMs of difference that show thinning here of up  
659 to  $55 \text{ m}$  between 1984–2018 CE (Fig. 3D and 3E) (King et al., 2020). Simulated surface elevation  
660 change in the ablation area was  $-30 \text{ m}$  over 20 years to the present day and similar to values derived  
661 from satellite observations for 1984–2018 CE (King et al., 2020). Simulated present-day glacier  
662 velocities (Fig. 9) reached a maximum of  $248 \text{ m a}^{-1}$  and showed a similar pattern and magnitude to  
663 glacier surface velocities observed using remote sensing observations, which reach a maximum of  $220$   
664  $\text{m a}^{-1}$  in the Khumbu Icefall (Altena and Kääh, 2020) and up to  $20 \text{ m a}^{-1}$  in the ablation area (Quincey  
665 et al., 2009; Dehecq et al. 2019). The simulated present-day velocities in this study were a better fit to

Deleted: mean annual air temperature

Deleted:

Formatted: Superscript

668 remote sensing observations than those from previous simulations that used an elevation-dependent  
669 mass balance forcing (Rowan et al., 2015, 2021) where the maximum simulated velocities were 118 m  
670 a<sup>-1</sup>.

### 671 3.5 Climate change and glacier evolution from the present day until 2100 CE

672 Khumbu Glacier is responding to historical climate change and will continue to shrink even if warming  
673 ceases today. Indeed, if we allow the spin-up experiment to reach equilibrium with the present-day  
674 NOAA RCM mass balance, the glacier terminus will recede by 2.1 km and the maximum ice thickness  
675 will decrease from 246 m to 206 m by 2100 CE without any additional warming. In this scenario, a  
676 supraglacial debris layer up to 1.3 m thick extends 1 km up-glacier from the terminus and partially  
677 dampens the committed volume loss, by sustaining 13% more ice volume than would be the possible  
678 for a clean-ice glacier surface with the same mass balance (Fig. 10A). The committed glacier volume  
679 loss due to historical warming in the absence of any further climate forcing is 10–23% of the present-  
680 day glacier mass (Fig. 10C) with the associated uncertainty represented by this range of values arising  
681 from the parameterisation of the impact of supraglacial debris evolution on surface melting.

682 Now considering the effects of additional warming under the RCP scenarios for the NOAA experiment,  
683 we find that greater warming occurs in winter than in the monsoon under both RCPs and results in an  
684 increase in annual precipitation amount of about 15% made up of a greater increase in non-monsoon  
685 precipitation than monsoon precipitation (Fig. 2E). The climate forcing from the downscaled NOAA  
686 RCM under RCP4.5 is 1.4°C warmer than the present day (–0.75°C in 2095–2100 CE compared with  
687 –2.15°C in 2015–2020 CE) and annual precipitation increases by 14.8% from 581.4 mm at present day  
688 to 664.8 mm a<sup>-1</sup> by 2100 CE with monsoon (June–September) precipitation increasing by 5.4% and  
689 non-monsoon season (December–February) precipitation increasing by 14.1% (Fig. 2E). Under  
690 RCP8.5, the downscaled climate forcing is projected to be 3.8°C warmer than present day (1.65°C in  
691 2095–2100 CE) with an increase in annual precipitation of 14.9% by 2100 CE, with monsoon  
692 precipitation increasing by 9.8% and non-monsoon precipitation increasing by 19.4% (Fig. 2E).

693 In the NOAA RCM RCP4.5 experiment, the spatially averaged cumulative glacier mass balance is –  
694 0.14 m w.e. a<sup>-1</sup> in 2100 CE, which is slightly more positive than the present-day value of –0.21 m w.e.  
695 a<sup>-1</sup> (Fig. 6) and glacier volume decreases by 36% between the present day and 2100 CE (Fig. 10C).  
696 While significant, this end-of-century glacier loss is partially offset by the concurrent increase in  
697 precipitation. In comparison, an equivalent simulation forced only by warming and without any change  
698 in precipitation results in a more linear trajectory of glacier change and 70% loss of glacier volume by  
699 2100 CE (cyan line in Fig. 10C) demonstrating that 34% of potential glacier loss from warming could  
700 be compensated by the increase in precipitation that occurs as a result of warming.

### 701 3.6 Comparison of projections for different RCM forcings

702 The CCCma and IPSL RCMs projected greater warming from the present day by 2100 CE than the  
703 NOAA RCM under RCP4.5 with a value of 1.6°C (+0.2°C compared with the NOAA RCM) in the IPSL  
704 RCM experiment and 2.2°C (+0.8°C) in the CCCma RCM experiment. These two RCMs also projected  
705 slightly greater warming by 2100 CE under RCP8.5, with a value of 3.9°C (+0.1°C compared with the  
706 NOAA RCM) for the IPSL RCM experiment and 4.1°C (+0.3°C) for the CCCma RCM experiment.

707 The projected increase in precipitation amount across the three RCMs is similar between RCPs with  
708 annual totals above 600 mm by 2100 CE. The CCCma RCM gives the greatest increase in annual  
709 precipitation amount of 100 mm by 2100 CE (Fig. 2E). There is no evidence of change in the intensity  
710 of the Indian Summer Monsoon, as the seasonal split in precipitation remains similar to the present day,  
711 but the frequency of days with high precipitation (over 15 mm per day) increases by 2100 CE, giving  
712 twice as many days in the NOAA RCM experiment and up to seven times as many days in the IPSL  
713 RCM experiment.

714 Under RCP8.5, all experiments showed similar results for mass balance by 2100 CE with only a 10%  
715 difference in glacier volume between the three RCMs (Fig. 10C). The CCCma RCM experiment has  
716 only a 1% difference in volume loss between RCP4.5 and RCP8.5 by 2100 CE despite a 1.9°C

Deleted: summer

Deleted: winter

Deleted: summer

Deleted: summer

Deleted: winter

Deleted: summer

Deleted: winter

730 difference in MAAT—this is a surprising result given the significant temperature difference, which can  
731 be attributed to the greater number of high-magnitude precipitation events that occur under RCP8.5 in  
732 combination with the small difference in winter temperatures between the two RCPs. Indeed, in the  
733 CCCma RCM experiment under RCP4.5, the maximum winter temperature is 1.7°C higher than for the  
734 other RCMs, resulting in ablation and rainfall (rather than snowfall) during the winter.

## 735 736 **4. Discussion**

### 737 **4.1 Uncertainties associated with the glacier modelling**

738 Sources of uncertainty in our results arose from each step of our glacier modelling workflow, and we  
739 considered how the experiments could be designed to reduce these uncertainties. Here we discuss the  
740 potential sources of uncertainty associated with the choice of RCMs, the downscaling of the RCMs, the  
741 use of time slices rather than continuous mass balance calculations, the representation of future  
742 precipitation in the RCMs, and the representation of avalanching in the glacier model.

743  
744 A single RCM was not considered sufficient to represent both present-day climate and potential future  
745 climatic extremes, but the climate-mass balance forcing ensemble was limited in size due to the small  
746 number of RCMs available. The use of three RCMs allowed the implications of uncertainties in  
747 understanding of local climate for glacier evolution to be evaluated. A multi-model mean approach  
748 using all the CORDEX South Asia RCMs (as widely used elsewhere) was not considered sufficient to  
749 represent present-day and future climate conditions in the Khumbu Valley because this approach gives  
750 equal weighting to models irrespective of their performance (Pierce et al., 2009) and does not enable  
751 intercomparison of results for future climate conditions.

752  
753 Five-year downscaled RCM time slices were chosen to reduce computational expense associated with  
754 COSIPY and the integration with iSOSIA. To ensure that the five-year periods selected were  
755 representative, the preceding decade was used for comparison with the time-slice results (results not  
756 shown). The use of quantile mapping with 14 years of AWS data as the downscaling method limited the  
757 influence of any natural variability by ensuring that the period did not reflect an extreme phase of natural  
758 climate oscillation. This comparison was particularly important for the future time slices, where large  
759 uncertainties arise between RCMs, and observational data cannot be used for evaluation of the  
760 downscaled climate or the resulting mass balance. We note that this experimental design could be  
761 improved by interpolating the mass balance over time and coupling the COSIPY and iSOSIA models  
762 such that mass balance was calculated dynamically for the evolving ice surface, but this was beyond  
763 the scope of our experiments. However, the experiments were repeated using additional mid-Century  
764 (2045–2050 CE) mass balance forcings to investigate if this produced a different end-of-Century result.  
765 These experiments produced near-identical results in 2100 CE to the experiments with no mid-Century  
766 forcing, in part because the response time of the simulated glaciers was longer than the 40-year period  
767 between the present-day and future time slices. Thus, a mid-century surface mass balance forcing was  
768 not considered necessary in our experiments and instead we used a step forcing for mass balance rather  
769 than interpolation between mass balance calculations in the glacier model.

770  
771 The differences in simulated glacier change and response time between RCM forcings were at times  
772 greater than those resulting from the RCP due to differences in projections of precipitation. Whilst the  
773 three selected RCMs performed well in representing annual precipitation cycles from the six available  
774 CORDEX RCMs, we note that this representation was still fairly poor, although substantially improved  
775 by quantile mapping (Fig. 2D). The poor representation of monsoon dynamics in the present-day RCMs  
776 highlights an additional uncertainty associated with future precipitation scenarios and that these results  
777 should be treated as a set of possible scenarios.

778  
779 The CORDEX CMIP5 and CMIP6 projects only produced dynamically downscaled RCMs for two  
780 future emissions scenarios (RCP4.5 and RCP8.5) and as such the implications of other RCPs for glacier  
781 evolution could not be assessed. The downscaled future climates were compared with those from other  
782 studies using CORDEX results, and showed similar annual and seasonal regional temperature trends  
783 strongly linked to the choice of RCP, and similar positive precipitation trends with poor agreement  
784 between RCMs (Kaini et al., 2019; Sanjay et al., 2017). The relationship between precipitation and

785 warming in the two future emissions scenarios was less clear than that for air temperatures because the  
786 monsoon-influenced Himalaya has particularly poor RCM consensus and high levels of uncertainty in  
787 future precipitation trends with warming relative to other regions in High Mountain Asia (Sanjay et al.,  
788 2017).

789  
790 A potentially large uncertainty in the glacier model arose from the parameterisation of avalanching, as  
791 this mass balance variable is poorly constrained, with no direct observations of the avalanche  
792 contribution to the mass balance of Khumbu Glacier and high regional variability (Kneib et al., 2025).  
793 Avalanching was included in iSOSIA by slope-dependent diffusion and resulted in increased  
794 accumulation along the glacier surface in the Western Cwm and improved the agreement between  
795 simulated and estimated accumulation rates and distribution (Fig. 1D). Future work to resolve the  
796 impact of low frequency–high magnitude avalanche events on accumulation rates would be useful to  
797 refine this calculation but the contribution of avalanches to glacier accumulation over decadal time  
798 scales remains extremely challenging to measure (Purdie et al., 2025).

Deleted: observed

#### 800 4.2 Impacts of mesoscale and microscale meteorology on glacier change

801 Our study addresses fine-scale temporal (hourly) and spatial (100 m) glacier surface processes,  
802 including avalanching and sublimation, that affect glacier surface mass balance across the elevation  
803 range of Khumbu Glacier, but further observations of meteorological and glaciological conditions at  
804 the highest elevations would be beneficial, and are needed if micro-scale processes are to be included  
805 in glacier models (Brun et al., 2023; Khadka et al., 2021; Mölg et al., 2014; Shaw et al., 2022). Analysis  
806 of meteorological observations from AWS across the Dudh Koshi catchment indicated that precipitation  
807 gradients were weak, slightly negative or absent, confirming the observations of Salerno et al. (2015)  
808 and Yang et al. (2017). To test the sensitivity of precipitation to elevation, COSIPY was forced by a  
809 gridded climate distributed using weak negative, weak positive, and no precipitation gradients  
810 distributed across the model domain using a linear regression with elevation from the 100-m resolution  
811 DEM. The results of these experiments were used to force iSOSIA and the simulated historical glacier  
812 evolution was similar, resulting in only a 10 m difference in the maximum ice thickness between  
813 simulations with different precipitation gradients (result not shown).

814  
815 The mass balance sensitivity to seasonal and daily variations in lapse rate showed a lesser impact on  
816 glacier-wide mass balance than in other studies, due to the large elevation range of Khumbu Glacier  
817 whereby a smaller fraction of the glacier relative to total area is located along the zero degree isotherm  
818 (e.g., compared to Yala Glacier in Nepal; Immerzeel et al., 2014). Seasonal and daily lapse rates that  
819 accounted for marked lower values during the monsoon season and at night gave a mean annual value  
820 of  $5.54\text{ }^{\circ}\text{C km}^{-1}$ , which produced glacier-wide mass balance and ice thickness simulations that were  
821 closest to geodetic observations and represented the maximum rates of surface lowering in the upper  
822 ablation area where the debris layer is thinnest (Fig. 3D and 3E).

823  
824 Sublimation simulated in our study occurred at all elevations with the highest rate of ice loss due to  
825 sublimation ( $-0.12\text{ m w.e. a}^{-1}$ ) in the upper reaches of the Khumbu Glacier catchment near to South Col  
826 (about 7,495 m a.s.l.) where sublimation dominated ablation with only minor seasonality (Fig. A6).  
827 Whilst this amount of ice loss by sublimation is not negligible, it is almost half that found in the point-  
828 based calculations after adjusting for the different time periods represented by our studies (Matthews et  
829 al., 2020), which is likely due to the assumed uniformity of wind speed across the model domain in  
830 COSIPY. Future work to improve the calculation of sublimation in distributed surface mass balance  
831 calculations for high-elevation glaciers would be valuable.

832  
833 While we have considered the effects of mesoscale meteorology on glacier mass balance, smaller-scale  
834 processes operating close to the land surface could also be important. Katabatic winds were suggested  
835 to explain a local 15-year decrease in maximum air temperatures and precipitation over glaciers while  
836 minimum air temperatures continued to rise (Salerno et al., 2023). However, this effect was found to be  
837 short-lived (Shaw et al., 2025) and the impact of microscale near-surface cooling on the duration and  
838 extent of mesoscale precipitation and accumulation is likely to be minimal and therefore unlikely to  
839 significantly affect glacier-wide mass balance (Mott et al., 2020; Shaw et al., 2024). Observations from

841 the Camp 2 AWS (6,464 m a.s.l.) indicate that surface energy fluxes may be sufficient to cause non-  
842 negligible melting of glacier surfaces despite freezing air temperatures (Matthews et al., 2020). Results  
843 from an ice core from South Col Glacier (>8,000 m a.s.l.) combined with COSIPY experiments  
844 suggested that ablation may also take place at even at the highest elevations (Potocki et al., 2022).  
845 However, a subsequent study found no evidence of glacier mass change, and identified large  
846 uncertainties associated with simulating mass balance at these extreme elevations where sub-daily air  
847 temperature gradients and the duration of snow cover strongly affect ablation and accumulation (Brun  
848 et al., 2023). Future work is needed to reduce these uncertainties, as very few observations exist of  
849 accumulation processes and the upper limit of ablation processes for high-elevation Himalayan glaciers.

850

#### 851 4.3 Possible outcomes under RCP8.5

852 Current global greenhouse gas emissions are following the trajectory of the intermediate emissions  
853 scenario RCP4.5, while the high emissions scenario RCP8.5 could be described as ‘low possibility but  
854 high impact’ (Pedersen et al., 2020). However, as represented in the RCMs used in our study, mountain  
855 regions are warming more rapidly than the global mean such that a global temperature rise of 1.5°C will  
856 lead to  $2.1 \pm 0.1^\circ\text{C}$  of warming in High Mountain Asia (Kraaijenbrink et al., 2017; Pepin et al., 2022)  
857 although the occurrence of elevation-dependent warming above 5,000 m a.s.l. is debated (Gao et al.,  
858 2018). The high temperatures projected under RCP8.5 could potentially be offset partly by increased  
859 precipitation, given that high-magnitude precipitation events from winter Westerly disturbances  
860 increased by a factor of seven between present day and 2100 CE in the IPSL RCM under RCP8.5.

861

862 We found no evidence of future increases in precipitation offsetting RCP8.5 warming; net glacier mass  
863 balance was strongly negative in all RCP8.5 experiments and insufficient to maintain any actively  
864 flowing glacier. Under RCP8.5, glacier mass balance in the monsoon-influenced Himalaya may  
865 therefore shift from being driven by accumulation during the monsoon to predominantly during winter.  
866 Monsoon precipitation would only result in snow accumulation at the very highest elevations and would  
867 be insufficient to maintain flowing glaciers. This outcome is avoidable by limiting anthropogenic  
868 warming to within RCP4.5, which, due to the associated increase in precipitation, could sustain nearly  
869 two thirds of the current glacier volume until 2100 CE and potentially for two centuries further into the  
870 future.

871

#### 872 4.4 Comparison with global glacier modelling results

873 A recent global glacier modelling study forced by an ensemble of 10 GCMs projected mass loss of 64%  
874 for Khumbu Glacier by 2100 CE (Rounce et al., 2023). In comparison, our experiments project less  
875 severe rates of decline, resulting in 30% less mass loss under the RCP4.5 future climate scenario than  
876 in the global study (Fig. 10C). One difference between these results is that rather than using the global  
877 glacier inventory outline to define the glacier margins we consider only the actively flowing glacier and  
878 so exclude 20% of the starting glacier volume in the detached tongue. We would expect the two sections  
879 of the glacier to evolve along different paths; while the active glacier responds to climate change as  
880 projected in our experiments, thick supraglacial debris mantling the detached tongue could allow this  
881 ice mass to survive and slowly decay *in situ* for many decades beyond the present day. The decay of the  
882 detached tongue may however increase due to erosion of the surface by ice cliffs and supraglacial water  
883 bodies that are expanding across the former glacier surface (King et al., 2020).

884

885 Our experiments only consider the rapidly changing active glacier, and we expect that the debris-  
886 covered tongue would melt more slowly than projected in the global modelling study, but as we do not  
887 consider the stagnant tongue to be part of the present-day glacier the ice volume simulated at the start  
888 of our experiments is smaller than that represented by Rounce et al. (2023) and other studies based on  
889 the RGI glacier inventory. The dynamically detached debris-covered tongue represents about 20% of  
890 the present-day glacier volume and contains ice estimated as up to 360 m thick. The mean present-day  
891 ablation rate across this section of the glacier simulated in Rowan et al. (2021) is  $-0.54 \text{ m w.e. a}^{-1}$  which  
892 can be used to estimate the life expectancy of the debris-covered tongue assuming no input of ice from  
893 the active glacier and no change in ablation rate due to thickening of supraglacial debris or the  
894 development of ice cliffs and supraglacial ponds. While the thickest part of the detached tongue may

895 survive for ~600 years, the mean life expectancy of this ice mass is  $176 \pm 148$  years from the present  
896 day meaning that the former debris-covered tongue will vanish by 2200 CE.  
897

#### 898 4.5 The response of large debris-covered glaciers to climate change

899 The dynamic response time of large glaciers to climate change is of the order of centuries. For this  
900 reason, we start our simulations from the late Holocene (~1 ka) moraine extent when Khumbu Glacier  
901 was last considered dynamically stable (Hornsey et al., 2022; Rowan et al., 2015). The relationship  
902 between glacier response time and mass balance becomes less important after 2100 CE when the glacier  
903 is so small that ice flow has little impact on glacier volume change. Global and regional glacier  
904 modelling studies typically start their simulations in the current Century (e.g., 2000–2007 CE in  
905 Marzeion et al. (2020); 2000 CE in Rounce et al. (2023)) and a further complication arises from the use  
906 of global glacier inventories as a starting point for glacier modelling studies as such inventories cannot  
907 capture the current dynamic state of glaciers that are imbalanced, and include all ice-covered areas  
908 rather than identifying only actively flowing ice. However, satellite-derived velocity products could be  
909 used identify where ice flow within glacier outlines declines to negligible rates (Dehecq et al., 2019).  
910

Deleted: 15

911 The RGI 7.0 inventory for Khumbu Glacier is based on imagery from 1999 CE (RGI 7.0 Consortium,  
912 2023) where the detached debris-covered tongue represents 20% of the glacier volume contained within  
913 this outline (Fig. 1C). Simulations that integrated the stagnant tongue into the model domain rather than  
914 as part of the flowing ice improved the representation of simulated ice flow compared to observed  
915 values, supporting our conclusion that the debris-covered tongue has been dynamically detached from  
916 the active glacier for 50–100 years (Rowan et al., 2021). Field observations support the concept of  
917 active and stagnant sections co-existing in contact with each other as englacial optical televiewing  
918 indicated that thrusting occurs at several sites, denoted by skewed internal debris layers and of basal ice  
919 that has been thrust to the glacier surface, near to the active glacier terminus from the direction of  
920 Khumbu Icefall (Miles et al., 2021). Our simulations show that development of supraglacial debris at  
921 the active glacier terminus reduced net volume loss by 13% (Fig. 8). Dynamic detachment of debris-  
922 covered tongues could allow these glaciers to move closer to equilibrium with a rapidly changing  
923 climate, the local mass balance gradient is a more important control on glacier change for both clean-  
924 ice glaciers and debris-covered Himalayan glaciers.  
925

#### 926 5. Conclusions

927 In the monsoon-influenced Himalaya, 85% of the glacier area is located higher than 5,000 m above sea  
928 level, and 21% of this ice is above 6000 m in elevation. Despite these high elevations, Himalayan  
929 glaciers are rapidly losing ice in response to recent warming and are projected to shrink by 53% to 70%  
930 during this Century. However, the impact of future changes in precipitation on glacier loss remains  
931 uncertain, because changes in precipitation amount and distribution is often overlooked in glacier model  
932 projections. We explored the effects of future warming in tandem with changes in precipitation by  
933 simulating the evolution of Khumbu Glacier in the Everest region of Nepal using a surface energy and  
934 mass balance model forced by downscaled Regional Climate Model outputs to drive an ice-dynamical  
935 glacier evolution model. Historical warming commits Khumbu Glacier to loss of 10–23% of the total  
936 ice volume by 2100 CE. While warming due to intermediate future greenhouse gas emissions (RCP4.5)  
937 will lead to glacier volume loss of 70% by 2100 CE, the projected concurrent increase in precipitation  
938 amount will offset 34% of this and so reduce glacier loss by about a half. However, high future  
939 emissions (RCP8.5) will not be compensated by changes in precipitation amount but will instead result  
940 in substantial ablation above 6,000 m with devastating consequences for one of the highest glaciers on  
941 Earth. Our results indicate that the net mass balance of Khumbu Glacier could be close to zero in 2100  
942 CE under RCP4.5 and therefore, if climate change is limited to this intermediate emissions scenario,  
943 Khumbu Glacier will recede to the base of the icefall with insignificant further change in glacier volume  
944 beyond this point. In this scenario, Khumbu Glacier has a similar extent in 2100 CE to the active section  
945 of the present-day glacier, and represents at least one example of how monsoon-influenced Himalayan  
946 glaciers could persist into the future if global efforts are sufficient to mitigate anthropogenic climate  
947 change.  
948

Deleted: ¶

949

952 **Code availability**  
953 The COSIPY version 1.3 glacier surface energy and mass balance model is available from the original  
954 publication describing this model (Sauter et al., 2020) and Zenodo (Arndt et al., 2020). The iSOSIA  
955 version spm-3.3.3r glacier model is available from Zenodo (Rowan and Pedersen, 2024).  
956

957 **Data availability**  
958 Daily data from the Coordinated Regional Downscaling Experiment (CORDEX) South Asia domain  
959 were downloaded from the Indian Institute of Tropical Meteorology website  
960 ([http://cccr.tropmet.res.in/home/cordexsa\\_about.jsp](http://cccr.tropmet.res.in/home/cordexsa_about.jsp)) for the grid box nearest to Khumbu Glacier  
961 (27.9065°N, 86.4353°E). Incoming shortwave and longwave radiation components were downloaded  
962 from the ESGF portal (<https://esgf-ui.ceda.ac.uk/cog/projects/cordex-ceda/>). Meteorological  
963 observations were derived from the Ev-K2-CNR SHARE network (<https://www.ev-k2cnr.org>) and the  
964 GlacioClim (<https://glacioclim.osug.fr/>).  
965

966 **Author contributions**  
967 Conceptualisation: DJQ, ANR, AVR  
968 Data curation: ASD, ANR, AVR  
969 Formal analysis: ASD, ANR, AVR  
970 Funding acquisition: DJQ, ANR, AVR  
971 Investigation: ASD  
972 Methodology: ASD, ANR, AVR, VKP  
973 Project administration: DJQ, ANR  
974 Resources: DJQ, ANR  
975 Software: AVR, VKP  
976 Supervision: DJQ, ANR, AVR  
977 Validation: ASD, AVR  
978 Visualisation: ASD, AVR  
979 Writing – original draft preparation: ASD, AVR, DJQ, ANR, VKP  
980 Writing – review and editing: ASD, AVR, DJQ, ANR, VKP  
981

982 **Competing interests**  
983 The authors declare that they have no conflicts of interest related to this work.  
984

985 **Acknowledgements**  
986 Tobias Sauter and Anselm Arndt are thanked for support in using COSIPY. We thank Patrick Wagon  
987 for sharing the Pyramid and Changri Nup Glacier automatic weather station data. We thank David  
988 Rounce for sharing the global glacier model results for Khumbu Glacier from Rounce et al. (2023). We  
989 thank Editor Emily Collier, Emily Potter and an anonymous reviewer for their detailed and constructive  
990 comments that greatly improved the focus and clarity of this work.  
991

992 **Financial support**  
993 ASD was supported by the Priestley International Centre for Climate at the University of Leeds, and a  
994 University of Leeds Anniversary Research Scholarship. AVR was supported by a Royal Society  
995 Dorothy Hodgkin Research Fellowship (DHF\R1\201113). Some of the simulations presented were  
996 performed using resources provided by Sigma2, the National Infrastructure for High-Performance  
997 Computing and Data Storage in Norway.  
998  
999

1000 **References**  
1001 Altna, B. and Käab, A.: Ensemble matching of repeat satellite images applied to measure fast-changing  
1002 ice flow, verified with mountain climber trajectories on Khumbu icefall, Mount Everest, *J.*  
1003 *Glaciol.*, 66, 905–915, <https://doi.org/10.1017/jog.2020.66>, 2020  
1004 Arndt, A., Sauter, T., Saß, B., [cryotoools/cosipy](https://github.com/cryotoools/cosipy): COSIPY v1.3 – An open-source coupled snowpack and  
1005 ice surface energy and mass balance model (v1.3). Zenodo.  
1006 <https://doi.org/10.5281/zenodo.3902191>, 2020

Deleted: .

Deleted: (2020)

Deleted: .

1010 Anderson, L. S. and Anderson, R. S.: Modeling debris-covered glaciers: response to steady debris  
1011 deposition, *The Cryosphere*, 10, 1105–1124, <https://doi.org/10.5194/tc-10-1105-2016>, 2016,  
1012 Bartlett, O. T., Ng, F. S. L., and Rowan, A. V.: Morphology and evolution of supraglacial hummocks on  
1013 debris-covered Himalayan glaciers, *Earth Surf. Process. Landforms*, 46, 525–539,  
1014 <https://doi.org/10.1002/esp.5043>, 2021.

1015 Benn, D. I. and Lehmkuhl, F.: Mass balance and equilibrium-line altitudes of glaciers in high-mountain  
1016 environments, *Quaternary International*, 65–66, 15–29, [https://doi.org/10.1016/S1040-6182\(99\)00034-8](https://doi.org/10.1016/S1040-6182(99)00034-8), 2000.

1017 Benn, D. I. and Owen, L. A.: The role of the Indian summer monsoon and the mid-latitude westerlies  
1018 in Himalayan glaciation: review and speculative discussion, *Journal of the Geological Society*,  
1019 155, 353–363, <https://doi.org/10.1144/gsjgs.155.2.0353>, 1998.

1020 Biemans, L.H. Speelman, F. Ludwig, E.J. Moors, A.J. Wiltshire, P. Kumar, D. Gerten, P., Kabat, P.,  
1021 Future water resources for food production in five South Asian river basins and potential for  
1022 adaptation—A modeling study, *Science of The Total Environment*,  
1023 <https://doi.org/10.1016/j.scitotenv.2013.05.092>, 2013.

1024 Bonekamp, P. N. J., Wanders, N., Wiel, K., Lutz, A. F., Immerzeel, W. W.: Using large ensemble  
1025 modelling to derive future changes in mountain specific climate indicators in a 2 and 3°C warmer  
1026 world in High Mountain Asia, *Int J Climatol*, 41, <https://doi.org/10.1002/joc.6742>, 2021.

1027 Bookhagen, B. and Burbank, D. W.: Topography, relief, and TRMM-derived rainfall variations along  
1028 the Himalaya, *Geophys. Res. Lett.*, 33, L08405, <https://doi.org/10.1029/2006GL026037>, 2006.

1029 Brock, B.W., Willis, I.C. and Sharp, M.J.: Measurement and parameterization of aerodynamic  
1030 roughness length variations at Haut Glacier d’Arolla, Switzerland. *Journal of Glaciology*,  
1031 52(177), pp.281-297. <https://doi.org/10.3189/172756506781828746>, 2006

1032 Brun, F., King, O., Réveillet, M., Amory, C., Planchot, A., Berthier, E., Dehecq, A., Bolch, T., Fourteau,  
1033 K., Brondex, J., Dumont, M., Mayer, C., Leinss, S., Hugonnet, R., and Wagnon, P.: Everest South  
1034 Col Glacier did not thin during the period 1984–2017, *The Cryosphere*, 17, 3251–3268,  
1035 <https://doi.org/10.5194/tc-17-3251-2023>, 2023.

1036 Collins, M., Knutti, R., and Arblaster, J.: Long-term Climate Change: Projections, Commitments and  
1037 Irreversibility. In: *Climate Change 2013: The Physical Science Basis. Contribution of Working  
1038 Group I to the Fifth Assessment Report of the Intergovernmental Panel on Climate Change*  
1039 [Stocker, T.F., D. Qin, G.-K. Plattner, M. Tignor, S.K. Allen, J. Boschung, A. Nauels, Y. Xia, V.  
1040 Bex and P.M. Midgley (eds.)]. Cambridge University Press, Cambridge, United Kingdom and  
1041 New York, NY, USA., 1–108., 2013.

1042 Compagno, L., Huss, M., Miles, E. S., McCarthy, M. J., Zekollari, H., Dehecq, A., Pellicciotti, F., and  
1043 Farinotti, D.: Modelling supraglacial debris-cover evolution from the single-glacier to the  
1044 regional scale: an application to High Mountain Asia, *The Cryosphere*, 16, 1697–1718,  
1045 <https://doi.org/10.5194/tc-16-1697-2022>, 2022.

1046 Cuffey, K.M. and Paterson, W.S.B.: *The physics of glaciers*. Academic Press, 2010.

1047 Dehecq, A., Gourmelen, N., Gardner, A. S., Brun, F., Goldberg, D., Nienow, P. W., Berthier, E., Vincent,  
1048 C., Wagnon, P., and Trouvé, E.: Twenty-first century glacier slowdown driven by mass loss in  
1049 High Mountain Asia, *Nature Geosci*, 12, 22–27, <https://doi.org/10.1038/s41561-018-0271-9>,  
1050 2019.

1051 Egholm, D. L., Knudsen, M. F., Clark, C. D., and Lesemann, J. E.: Modeling the flow of glaciers in  
1052 steep terrains: The integrated second-order shallow ice approximation (iSOSIA), *J. Geophys.*  
1053 *Res.*, 116, <https://doi.org/10.1029/2010JF001900>, 2011.

1054 Farinotti, D., Huss, M., Fürst, J. J., Landmann, J., Machguth, H., Maussion, F., and Pandit, A.: A  
1055 consensus estimate for the ice thickness distribution of all glaciers on Earth, *Nat. Geosci.*, 12,  
1056 168–173, <https://doi.org/10.1038/s41561-019-0300-3>, 2019.

1057 Farr, T. G., Rosen, P. A., Caro, E., Crippen, R., Duren, R., Hensley, S., Kobrick, M., Paller, M.,  
1058 Rodriguez, E., Roth, L., Seal, D., Shaffer, S., Shimada, J., Umland, J., Werner, M., Oskin, M.,  
1059 Burbank, D., and Alsdorf, D.: The Shuttle Radar Topography Mission, *Reviews of Geophysics*,  
1060 45, 2005RG000183, <https://doi.org/10.1029/2005RG000183>, 2007.

1061 Ferguson, J. and Vieli, A.: Modelling steady states and the transient response of debris-covered glaciers,  
1062 *Cryosphere*, <https://doi.org/10.5194/tc-2020-228>, 2020.

1063

Deleted: .

Deleted: .

Deleted: .

Deleted: .

Deleted: P.

Deleted: (2013)

Deleted: .

Deleted: and

Deleted: .

Deleted: .

Deleted: , 2006.

Deleted: .

Deleted: .

Deleted: .

Deleted: , 2010.

Deleted: .

Deleted: .

Deleted: .

Deleted: .

Deleted: .

Deleted: .

1085 Förster, K., Hanzer, F., Winter, B., Marke, T., and Strasser, U.: An open-source MEteoroLOGical  
1086 observation time series DISaggregation Tool (MELODIST v0.1.1), *Geosci. Model Dev.*, 9, 2315–  
1087 2333, <https://doi.org/10.5194/gmd-9-2315-2016>, 2016. Deleted: .

1088 Gades, A., Conway, H., Nereson, N., Naito, N., and Kadota, T.: Radio echo-sounding through  
1089 supraglacial debris on Lirung and Khumbu Glaciers, Nepal Himalayas, *Debris-Covered Glaciers*  
1090 (Proceedings of a workshop held at Seattle, Washington, USA, September 2000). IAHS, 264, 13–  
1091 22, 2000. Deleted: .

1092 Gao, Y., Chen, F., Lettenmaier, D. P., Xu, J., Xiao, L., and Li, X.: Does elevation-dependent warming  
1093 hold true above 5000 m elevation? Lessons from the Tibetan Plateau, *npj Clim Atmos Sci*, 1, 19,  
1094 <https://doi.org/10.1038/s41612-018-0030-z>, 2018. Deleted: .

1095 Gromke, C., Manes, C., Walter, B., Lehning, M. and Guala, M.: Aerodynamic roughness length of fresh  
1096 snow. *Boundary-Layer Meteorology*, 141, pp.21-34. <https://doi.org/10.1007/s10546-011-9623-3>,  
1097 2011. Deleted: , 2011.

1098 Guo, S., Chen, R., Liu, G., Han, C., Song, Y., Liu, J., Yang, Y., Liu, Z., Wang, X., Liu, X. and Wang, L.:  
1099 Simple parameterization of aerodynamic roughness lengths and the turbulent heat fluxes at the  
1100 top of midlatitude August-One Glacier, Qilian Mountains, China. *Journal of Geophysical*  
1101 *Research: Atmospheres*, 123(21), pp.12-066. <https://doi.org/10.1029/2018JD028875>, 2018  
1102 Herreid, S. and Pellicciotti, F.: The state of rock debris covering Earth’s glaciers, *Nat. Geosci.*, 13, 621–  
1103 627, <https://doi.org/10.1038/s41561-020-0615-0>, 2020. Deleted: .

1104 Hornsey, J., Rowan, A. V., Kirkbride, M. P., Livingstone, S. J., Fabel, D., Rodes, A., Quincey, D. J.,  
1105 Hubbard, B., and Jomelli, V.: Be-10 Dating of Ice-Marginal Moraines in the Khumbu Valley,  
1106 Nepal, Central Himalaya, Reveals the Response of Monsoon-Influenced Glaciers to Holocene  
1107 Climate Change, *JGR Earth Surface*, 127, <https://doi.org/10.1029/2022JF006645>, 2022. Deleted: .

1108 Huintjes, E., Neckel, N., Hochschild, V., and Schneider, C.: Surface energy and mass balance at  
1109 Purogangri ice cap, central Tibetan Plateau, 2001–2011, *J. Glaciol.*, 61, 1048–1060,  
1110 <https://doi.org/10.3189/2015JG15J056>, 2015. Deleted: .

1111 Immerzeel, W. W., van Beek, L. P. H., Konz, M., Shrestha, A. B., and Bierkens, M. F. P.: Hydrological  
1112 response to climate change in a glacierized catchment in the Himalayas, *Climatic Change*, 110,  
1113 721–736, <https://doi.org/10.1007/s10584-011-0143-4>, 2012. Deleted: .

1114 Irvine-Fynn, T.D., Sanz-Ablanedo, E., Rutter, N., Smith, M.W. and Chandler, J.H.: Measuring glacier  
1115 surface roughness using plot-scale, close-range digital photogrammetry. *Journal of Glaciology*,  
1116 60(223), pp.957-969. doi:10.3189/2014JG14J032, 2014. Deleted: , 2014.

1117 Jouvett, G., Huss, M., Funk, M., and Blatter, H.: Modelling the retreat of Grosser Aletschgletscher,  
1118 Switzerland, in a changing climate, *J. Glaciol.*, 57, 1033–1045,  
1119 <https://doi.org/10.3189/002214311798843359>, 2011. Deleted: .

1120 Kaini, S., Nepal, S., Pradhananga, S., Gardner, T. and Sharma, A. K.: Representative general circulation  
1121 models selection and downscaling of climate data for the transboundary Koshi river basin in  
1122 China and Nepal. *International Journal of Climatology*, 40(9): 4131-4149. doi: 10.1002/joc.6447,  
1123 2019. Deleted: .

1124 Katzenberger, A., Schewe, J., Pongratz, J., and Levermann, A.: Robust increase of Indian monsoon  
1125 rainfall and its variability under future warming in CMIP6 models, *Earth Syst. Dynam.*, 12, 367–  
1126 386, <https://doi.org/10.5194/esd-12-367-2021>, 2021.

1127 Khadka, A., Matthews, T., Perry, L. B., Koch, I., Wagnon, P., Shrestha, D., Sherpa, T. C., Aryal, D., Tait,  
1128 A., Sherpa, T. G., Tuladhar, S., Baidya, S. K., Elvin, S., Elmore, A. C., Gajurel, A., and Mayewski,  
1129 P. A.: Weather On Mount Everest, During The 2019 Summer Monsoon, *Weather*, 76, 205–207,  
1130 <https://doi.org/10.1002/wea.3931>, 2021. Deleted: MOUNT EVEREST  
Deleted: MONSOON

1131 King, O., Bhattacharya, A., Ghuffar, S., Tait, A., Guilford, S., Elmore, A. C., and Bolch, T.: Six Decades  
1132 of Glacier Mass Changes around Mt. Everest Are Revealed by Historical and Contemporary  
1133 Images, *One Earth*, 3, 608–620, <https://doi.org/10.1016/j.oneear.2020.10.019>, 2020.

1134 Knap, W.H. and Oerlemans, J.: The surface albedo of the Greenland ice sheet: satellite-derived and in  
1135 situ measurements in the Søndre Strømfjord area during the 1991 melt season. *Journal of*  
1136 *Glaciology*, 42(141), pp.364-374. doi:10.3189/S0022143000004214, 1996. Deleted: , 1996.  
Deleted: .

1137 Kneib, M., Maussion, F., Brun, F., Carcanade, G., Farinotti, D., Huss, M., Van Tiel, M., Jouberton, A.,  
1138 Schmitt, P., Schuster, L., Dehecq, A., and Champollion, N.: Topographically-controlled

1156 contribution of avalanches to glacier mass balance in the 21st century, *Nat Commun*, 16, 10122,  
1157 <https://doi.org/10.1038/s41467-025-65608-z>, 2025.

1158 Kraaijenbrink, P. D. A., Bierkens, M. F. P., Lutz, A. F., and Immerzeel, W. W.: Impact of a global  
1159 temperature rise of 1.5 degrees Celsius on Asia's glaciers, *Nature*, 549, 257–260,  
1160 <https://doi.org/10.1038/nature23878>, 2017.

1161 Lafon, T., Dadson, S., Buys, G. and Prudhomme, C.: Bias correction of daily precipitation simulated by  
1162 a regional climate model: a comparison of methods. *International journal of climatology*, 33(6),  
1163 pp.1367-1381, 2013.

1164 Laha, S., Kumari, R., Singh, S., Mishra, A., Sharma, T., Banerjee, A., Nainwal, H. C., and Shankar, R.:  
1165 Evaluating the contribution of avalanching to the mass balance of Himalayan glaciers, *Ann.*  
1166 *Glaciol.*, 58, 110–118, <https://doi.org/10.1017/aog.2017.27>, 2017.

1167 Luo, M., Liu, T., Meng, F., Duan, Y., Frankl, A., Bao, A. and De Maeyer, P.: Comparing bias correction  
1168 methods used in downscaling precipitation and temperature from regional climate models: A case  
1169 study from the Kaidu River basin in western China. *Water*. 10(8), pp. 1046.  
1170 <https://doi.org/10.3390/w10081046>, 2018.

1171 Lutz, A.F., Immerzeel, W.W., Kraaijenbrink, P.D., Shrestha, A.B. and Bierkens, M.F.: Climate change  
1172 impacts on the upper Indus hydrology: sources, shifts and extremes. *PloS one*, 11(11),  
1173 p.e0165630, 2016.

1174 Marzeion, B., Hock, R., Anderson, B., Bliss, A., Champollion, N., Fujita, K., Huss, M., Immerzeel, W.  
1175 W., Kraaijenbrink, P., Malles, J., Maussion, F., Radić, V., Rounce, D. R., Sakai, A., Shannon, S.,  
1176 Van De Wal, R., and Zekollari, H.: Partitioning the Uncertainty of Ensemble Projections of  
1177 Global Glacier Mass Change, *Earth's Future*, 8, e2019EF001470,  
1178 <https://doi.org/10.1029/2019EF001470>, 2020.

1179 Maraun, D.: Bias correcting climate change simulations-a critical review. *Current Climate Change*  
1180 *Reports*, 2(4), pp.211-220, 2016.

1181 Matthews, T., Perry, L. B., Koch, I., Aryal, D., Khadka, A., Shrestha, D., Abernathy, K., Elmore, A. C.,  
1182 Seimon, A., Tait, A., Elvin, S., Tuladhar, S., Baidya, S. K., Potocki, M., Birkel, S. D., Kang, S.,  
1183 Sherpa, T. C., Gajurel, A., and Mayewski, P. A.: Going to Extremes: Installing the World's  
1184 Highest Weather Stations on Mount Everest, *Bulletin of the American Meteorological Society*,  
1185 101, E1870–E1890, <https://doi.org/10.1175/BAMS-D-19-0198.1>, 2020.

1186 Maurer, J. M., Schaefer, J. M., Rupper, S., and Corley, A.: Acceleration of ice loss across the Himalayas  
1187 over the past 40 years, *Sci. Adv.*, 5, eaav7266, <https://doi.org/10.1126/sciadv.aav7266>, 2019.

1188 Miles, E. S., Willis, I., Buri, P., Steiner, J. F., Arnold, N. S., and Pellicciotti, F.: Surface Pond Energy  
1189 Absorption Across Four Himalayan Glaciers Accounts for 1/8 of Total Catchment Ice Loss,  
1190 *Geophys. Res. Lett.*, 45, <https://doi.org/10.1029/2018GL079678>, 2018a.

1191 Miles, K. E., Hubbard, B., Quincey, D. J., Miles, E. S., Sherpa, T. C., Rowan, A. V., and Doyle, S. H.:  
1192 Polythermal structure of a Himalayan debris-covered glacier revealed by borehole thermometry,  
1193 *Sci Rep*, 8, 16825, <https://doi.org/10.1038/s41598-018-34327-5>, 2018b.

1194 Miles, K. E., Hubbard, B., Miles, E. S., Quincey, D. J., Rowan, A. V., Kirkbride, M., and Hornsey, J.:  
1195 Continuous borehole optical televiewing reveals variable englacial debris concentrations at  
1196 Khumbu Glacier, Nepal, *Commun Earth Environ*, 2, 12, <https://doi.org/10.1038/s43247-020-00070-x>, 2021.

1198 Miles, K. E., Hubbard, B., Miles, E. S., Quincey, D. J., and Rowan, A. V.: Internal structure of a  
1199 Himalayan debris-covered glacier revealed by borehole optical televiewing, *J. Glaciol.*, 1–12,  
1200 <https://doi.org/10.1017/jog.2022.100>, 2022.

1201 Mölg, T., Maussion, F., Yang, W. and Scherer, D.: The footprint of Asian monsoon dynamics in the mass  
1202 and energy balance of a Tibetan glacier. *The Cryosphere*, 6(6), pp.1445-1461.  
1203 <https://doi.org/10.5194/tc-6-1445-2012>, 2012.

1204 Mölg, T., Maussion, F., and Scherer, D.: Mid-latitude westerlies as a driver of glacier variability in  
1205 monsoonal High Asia, *Nature Clim Change*, 4, 68–73, <https://doi.org/10.1038/nclimate2055>,  
1206 2014.

1207 Mott, R., Stiperski, I., and Nicholson, L.: Spatio-temporal flow variations driving heat exchange  
1208 processes at a mountain glacier, *The Cryosphere*, 14, 4699–4718, <https://doi.org/10.5194/tc-14-4699-2020>, 2020.

Deleted: , 2013.

Deleted: .

Deleted: . 2018.

Deleted:

Deleted: , 201

Deleted: 6.

Deleted: .

Deleted: , 2016.

Deleted: .

Deleted: , 2012.

1220 Nakawo, M.: Processes Which Distribute Supraglacial Debris On The Khumbu Glacier, Nepal  
1221 Himalaya, *Annals of Glaciology*, 8, 1986.  
1222 Nicholson, L., Wirbel, A., Mayer, C., and Lambrecht, A.: The Challenge of Non-Stationary Feedbacks  
1223 in Modeling the Response of Debris-Covered Glaciers to Climate Forcing, *Front. Earth Sci.*, 9,  
1224 662695, <https://doi.org/10.3389/feart.2021.662695>, 2021.  
1225 Oerlemans, J.: *Glaciers and climate change*. CRC Press, 2001.  
1226 Owen, L. A., Robinson, R., Benn, D. I., Finkel, R. C., Davis, N. K., Yi, C., Putkonen, J., Li, D., and  
1227 Murray, A. S.: Quaternary glaciation of Mount Everest, *Quaternary Science Reviews*, 28, 1412–  
1228 1433, <https://doi.org/10.1016/j.quascirev.2009.02.010>, 2009.  
1229 Pedersen, J. S. T., Van Vuuren, D. P., Aparicio, B. A., Swart, R., Gupta, J., and Santos, F. D.: Variability  
1230 in historical emissions trends suggests a need for a wide range of global scenarios and regional  
1231 analyses, *Commun Earth Environ*, 1, 41, <https://doi.org/10.1038/s43247-020-00045-y>, 2020.  
1232 Pellicciotti, F., Stephan, C., Miles, E., Herreid, S., Immerzeel, W. W., and Bolch, T.: Mass-balance  
1233 changes of the debris-covered glaciers in the Langtang Himal, Nepal, from 1974 to 1999, *J.*  
1234 *Glaciol.*, 61, 373–386, <https://doi.org/10.3189/2015JoG13J237>, 2015.  
1235 Pepin, N. C., Arnone, E., Gobiet, A., Haslinger, K., Kotlarski, S., Notarnicola, C., Palazzi, E., Seibert,  
1236 P., Serafin, S., Schöner, W., Terzago, S., Thornton, J. M., Vuille, M., and Adler, C.: Climate  
1237 Changes and Their Elevational Patterns in the Mountains of the World, *Reviews of Geophysics*,  
1238 60, <https://doi.org/10.1029/2020RG000730>, 2022.  
1239 Piani, C., Weedon, G.P., Best, M., Gomes, S.M., Viterbo, P., Hagemann, S. and Haerter, J.O.: Statistical  
1240 bias correction of global simulated daily precipitation and temperature for the application of  
1241 hydrological models. *Journal of hydrology*, 395(3-4), pp.199-215.  
1242 <https://doi.org/10.1016/j.jhydrol.2010.10.024>, 2010  
1243 Pierce, D. W., Barnett, T. P., Santer, B. D., and Gleckler, P. J.: Selecting global climate models for  
1244 regional climate change studies, *Proc. Natl. Acad. Sci. U.S.A.*, 106, 8441–8446,  
1245 <https://doi.org/10.1073/pnas.0900094106>, 2009.  
1246 Potocki, M., Mayewski, P. A., Matthews, T., Perry, L. B., Schwikowski, M., Tait, A. M., Korotkikh, E.,  
1247 Clifford, H., Kang, S., Sherpa, T. C., Singh, P. K., Koch, I., and Birkel, S.: Mt. Everest’s highest  
1248 glacier is a sentinel for accelerating ice loss, *npj Clim Atmos Sci*, 5, 7,  
1249 <https://doi.org/10.1038/s41612-022-00230-0>, 2022.  
1250 Pritchard, H. D.: Asia’s shrinking glaciers protect large populations from drought stress, *Nature*, 569,  
1251 649–654, <https://doi.org/10.1038/s41586-019-1240-1>, 2019.  
1252 Purdie, H., Kerr, T., Robson, B., Anderson, B., Lorrey, A. M., Rack, W., Brasington, J., and Bealing, P.:  
1253 Mass balance characteristics of the ‘vanishing’ Rolleston Glacier, New Zealand, *Ann. Glaciol.*,  
1254 66, e31, <https://doi.org/10.1017/aog.2025.10032>, 2025.  
1255 Quincey, D. J., Luckman, A., and Benn, D.: Quantification of Everest region glacier velocities between  
1256 1992 and 2002, using satellite radar interferometry and feature tracking, *J. Glaciol.*, 55, 596–606,  
1257 <https://doi.org/10.3189/002214309789470987>, 2009.  
1258 Ragettli, S., Immerzeel, W. W., and Pellicciotti, F.: Contrasting climate change impact on river flows  
1259 from high-altitude catchments in the Himalayan and Andes Mountains, *Proc Natl Acad Sci USA*,  
1260 113, 9222–9227, <https://doi.org/10.1073/pnas.1606526113>, 2016.  
1261 RGI 7.0 Consortium: A Dataset of Global Glacier Outlines, Version 7.0. Boulder, Colorado USA.  
1262 NSIDC: National Snow and Ice Data Center, <https://doi.org/10.5067/f6jmovy5navz>, 2023.  
1263 Reiter, P., Gutjahr, O., Schefczyk, L., Heinemann, G. and Casper, M.: Does applying quantile mapping  
1264 to subsamples improve the bias correction of daily precipitation?. *International Journal of*  
1265 *Climatology*, 38(4), pp.1623-1633, 2018.  
1266 Roering, J. J., Kirchner, J. W., and Dietrich, W. E.: Evidence for nonlinear, diffusive sediment transport  
1267 on hillslopes and implications for landscape morphology, *Water Resources Research*, 35, 853–  
1268 870, <https://doi.org/10.1029/1998WR900090>, 1999.  
1269 Rounce, D. R., Hock, R., Maussion, F., Hugonnet, R., Kochtitzky, W., Huss, M., Berthier, E.,  
1270 Brinkerhoff, D., Compagno, L., Copland, L., Farinotti, D., Menounos, B., and McNabb, R. W.:  
1271 Global glacier change in the 21st century: Every increase in temperature matters, *Science*, 379,  
1272 78–83, <https://doi.org/10.1126/science.abo1324>, 2023.

Deleted: , 2001.

Deleted: .

Deleted: 201

Deleted: 0.

Deleted: , 2018.

Deleted: .

1279 Rowan, A. V.: The ‘Little Ice Age’ in the Himalaya: A review of glacier advance driven by Northern  
1280 Hemisphere temperature change, *The Holocene*, 27, 292–308,  
1281 <https://doi.org/10.1177/0959683616658530>, 2017.

1282 Rowan, A. V., Egholm, D. L., Quincey, D. J., and Glasser, N. F.: Modelling the feedbacks between mass  
1283 balance, ice flow and debris transport to predict the response to climate change of debris-covered  
1284 glaciers in the Himalaya, *Earth and Planetary Science Letters*, 430, 427–438,  
1285 <https://doi.org/10.1016/j.epsl.2015.09.004>, 2015.

1286 Rowan, A. V., Egholm, D. L., Quincey, D. J., Hubbard, B., King, O., Miles, E. S., Miles, K. E., and  
1287 Hornsey, J.: The Role of Differential Ablation and Dynamic Detachment in Driving Accelerating  
1288 Mass Loss From a Debris-Covered Himalayan Glacier, *J. Geophys. Res. Earth Surf.*, 126,  
1289 <https://doi.org/10.1029/2020JF005761>, 2021.

1290 Rowan, A., & Pedersen, V. K.: [annvrowan/isosia: iSOSIA version used in Schlich-Davies et al. \(spm-  
1291 3.3.3r\)](https://doi.org/10.5281/zenodo.12666864). Zenodo. <https://doi.org/10.5281/zenodo.12666864>, 2024

1292 Salerno, F., Guyennon, N., Yang, K., Shaw, T. E., Lin, C., Colombo, N., Romano, E., Gruber, S., Bolch,  
1293 T., Alessandri, A., Cristofanelli, P., Putero, D., Diolaiuti, G., Tartari, G., Verza, G., Thakuri, S.,  
1294 Balsamo, G., Miles, E. S., and Pellicciotti, F.: Local cooling and drying induced by Himalayan  
1295 glaciers under global warming, *Nat. Geosci.*, 16, 1120–1127, [https://doi.org/10.1038/s41561-  
1297 023-01331-y](https://doi.org/10.1038/s41561-<br/>
1296 023-01331-y), 2023.

1297 Sanjay, J., Krishnan, R., Shrestha, A. B., Rajbhandari, R., and Ren, G.-Y.: Downscaled climate change  
1298 projections for the Hindu Kush Himalayan region using CORDEX South Asia regional climate  
1299 models, *Advances in Climate Change Research*, 8, 185–198,  
1300 <https://doi.org/10.1016/j.accre.2017.08.003>, 2017.

1301 Sauter, T., Arndt, A., and Schneider, C.: COSIPY v1.3 – an open-source coupled snowpack and ice  
1302 surface energy and mass balance model, *Geosci. Model Dev.*, 13, 5645–5662,  
1303 <https://doi.org/10.5194/gmd-13-5645-2020>, 2020.

1304 Shaw, T. E., Miles, E. S., Chen, D., Jouberton, A., Kneib, M., Fugger, S., Ou, T., Lai, H.-W., Fujita, K.,  
1305 Yang, W., Fatichi, S., and Pellicciotti, F.: Multi-decadal monsoon characteristics and glacier  
1306 response in High Mountain Asia, *Environ. Res. Lett.*, 17, 104001, [https://doi.org/10.1088/1748-  
1308 9326/ac9008](https://doi.org/10.1088/1748-<br/>
1307 9326/ac9008), 2022.

1308 Shaw, T. E., Buri, P., McCarthy, M., Miles, E. S., and Pellicciotti, F.: Local Controls on Near-Surface  
1309 Glacier Cooling Under Warm Atmospheric Conditions, *JGR Atmospheres*, 129, e2023JD040214,  
1310 <https://doi.org/10.1029/2023JD040214>, 2024.

1311 Shaw, T. E., Miles, E. S., McCarthy, M., Buri, P., Guyennon, N., Salerno, F., Carturan, L., Brock, B.,  
1312 and Pellicciotti, F.: Mountain glaciers recouple to atmospheric warming over the twenty-first  
1313 century, *Nat. Clim. Chang.*, 15, 1212–1218, <https://doi.org/10.1038/s41558-025-02449-0>, 2025.

1314 Shea, J. M., Immerzeel, W. W., Wagnon, P., Vincent, C., and Bajracharya, S.: Modelling glacier change  
1315 in the Everest region, Nepal Himalaya, *The Cryosphere*, 9, 1105–1128,  
1316 <https://doi.org/10.5194/tc-9-1105-2015>, 2015.

1317 Sherpa, S. F., Wagnon, P., Brun, F., Berthier, E., Vincent, C., Lejeune, Y., et al.: Contrasted surface mass  
1318 balances of debris-free glaciers observed between the southern and the inner parts of the Everest  
1319 region (2007–15). *Journal of Glaciology*, 63(240), 637–651. <https://doi.org/10.1017/jog.2017.30>,  
1320 2017

1321 Strickland, R. M., Covington, M. D., Gulley, J. D., Kayastha, R. B., and Blackstock, J. M.: Englacial  
1322 Drainage Drives Positive Feedback Depression Growth on the Debris-Covered Ngozumpa  
1323 Glacier, Nepal, *Geophysical Research Letters*, 50, e2023GL104389,  
1324 <https://doi.org/10.1029/2023GL104389>, 2023.

1325 Vacco, D. A., Alley, R. B., and Pollard, D.: Glacial advance and stagnation caused by rock avalanches,  
1326 *Earth and Planetary Science Letters*, 294, 123–130, <https://doi.org/10.1016/j.epsl.2010.03.019>,  
1327 2010.

1328 Wagnon, P., Lafaysse, M., Lejeune, Y., Maisincho, L., Rojas, M. and Chazarin, J.P.: Understanding and  
1329 modeling the physical processes that govern the melting of snow cover in a tropical mountain  
1330 environment in Ecuador. *Journal of Geophysical Research: Atmospheres*, 114(D19), 2009,  
1331 <https://doi.org/10.1029/2009JD012811>, 2009.

1332 Watson, C. S., Quincey, D. J., Smith, M. W., Carrivick, J. L., Rowan, A. V., and James, M. R.:  
1333 Quantifying ice cliff evolution with multi-temporal point clouds on the debris-covered Khumbu  
1334 Glacier, Nepal, *J. Glaciol.*, 63, 823–837, <https://doi.org/10.1017/jog.2017.47>, 2017.

Deleted: (2024)

Deleted: .

Deleted: (2017).

Deleted: , 2009.

Deleted: .

1339 Weidemann, S.S., Sauter, T., Malz, P., Jaña, R., Arigony-Neto, J., Casassa, G. and Schneider, C.: Glacier  
1340 Mass Changes of Lake-Terminating Grey and Tyndall Glaciers at the Southern Patagonia Icefield  
1341 Derived From Geodetic Observations and Energy and Mass Balance Modeling. *Frontiers in Earth*  
1342 *Science*, 6: 81. doi: 10.3389/feart.2018.00081, 2018.  
1343 Wirbel, A., Jarosch, A. H., and Nicholson, L.: Modelling debris transport within glaciers by advection  
1344 in a full-Stokes ice flow model, *The Cryosphere*, 12, 189–204, [https://doi.org/10.5194/tc-12-189-](https://doi.org/10.5194/tc-12-189-2018)  
1345 2018, 2018.  
1346 Zekollari, H., Huss, M., Farinotti, D., and Lhermitte, S.: Ice-Dynamical Glacier Evolution Modeling—  
1347 A Review, *Reviews of Geophysics*, 60, <https://doi.org/10.1029/2021RG000754>, 2022.  
1348

1349

Deleted: (2018).

1351 **Tables and captions**

1352

1353 Table 1. Regional Climate Models (RCMs) chosen for this study and details of the Global Circulation  
 1354 Models (GCMs) from which these are derived.

1355

1356

CORDEX South Asia regional climate model	Driving CMIP5 global climate model	CMIP5 modelling centre	RCM name in this study	Future precipitation scenario (qualitative)	2100 CE mean temperature change from present day (°C)	
					RCP 4.5	RCP 8.5
ITM-RegCM4	NOAA-GFDL-GFDL-ESM2M	National Oceanic and Atmospheric Administration (NOAA), USA	NOAA	Wet	1.4	3.8
ITM-RegCM4	CCCma-CanESM2	Canadian Centre for Climate Modelling and Analysis (CCCma), Canada	CCCma	Moderate	2.2	4.1
ITM-RegCM4	IPSL-CMSA-LR	Institut Pierre-Simon Laplace (IPSL), France	IPSL	Dry	1.6	3.8

1357

1358

1359 Table 2: COSIPY model parameters, where  $\alpha$  is albedo (of fresh snow, firm and ice),  $t^*$  decay time from  
 1360 snow to firm,  $d^*$  the constant for the effect of snow depth on albedo, and  $z_0$  surface roughness length.

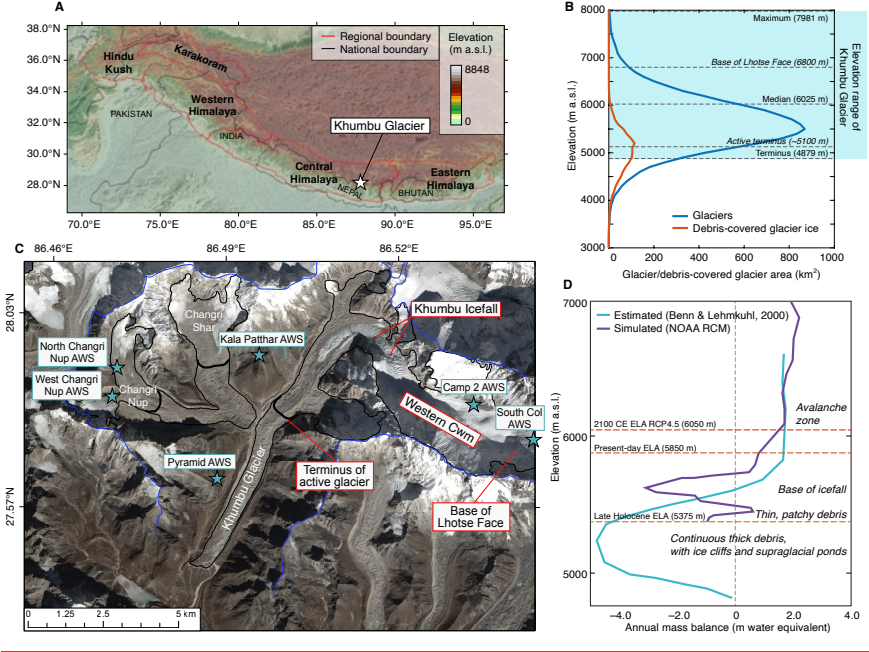
1361

Parameter	Value	Unit	Source
$\alpha_{\text{freshsnow}}$	0.85	-	Mölg et al. 2012; Wagnon et al., 2009
$\alpha_{\text{firm}}$	0.6	-	Knap and Oerlemans, 1996; Mölg et al. 2012
$\alpha_{\text{ice}}$	0.3	-	Mölg et al. 2012
$t^*$	20	days	Mölg et al. 2012
$d^*$	1.0	cm	Mölg et al. 2012
$Z_{0\text{snow}}$	0.24	mm	Gromke et al., 2011
$Z_{0\text{firm}}$	4.0	mm	Brock et al., 2006
$Z_{0\text{ice}}$	1.7	mm	Brock et al., 2006
$Z_0$ ageing length (linearly from $Z_{0\text{snow}}$ to $Z_{0\text{firm}}$ )	60	days	Mölg et al. 2012

1362

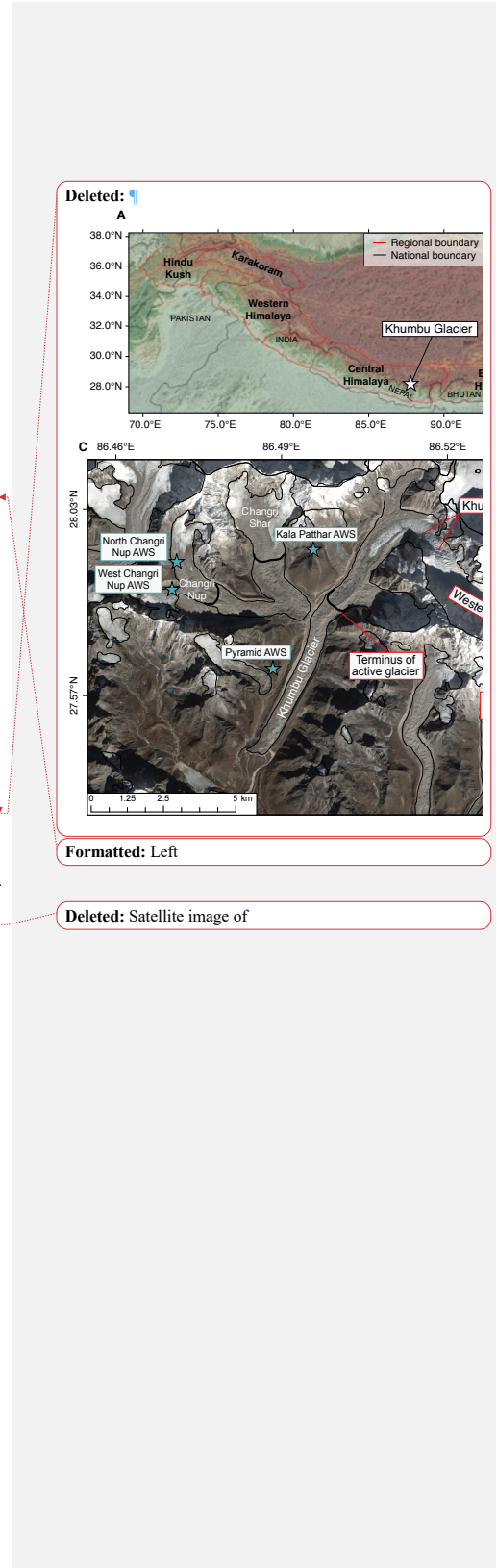
1363  
1364

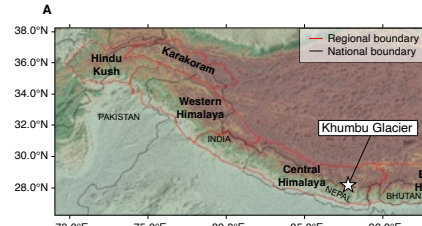
Figures and captions



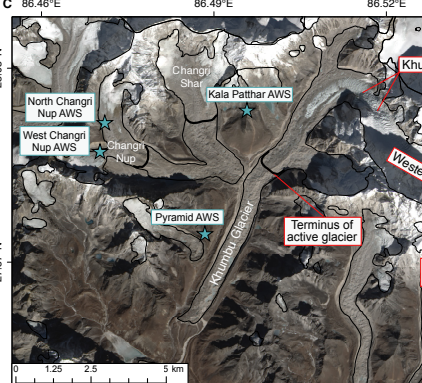
1365  
1366  
1367  
1368  
1369  
1370  
1371  
1372  
1373  
1374  
1375  
1376  
1377  
1378  
1379  
1380  
1381  
1382

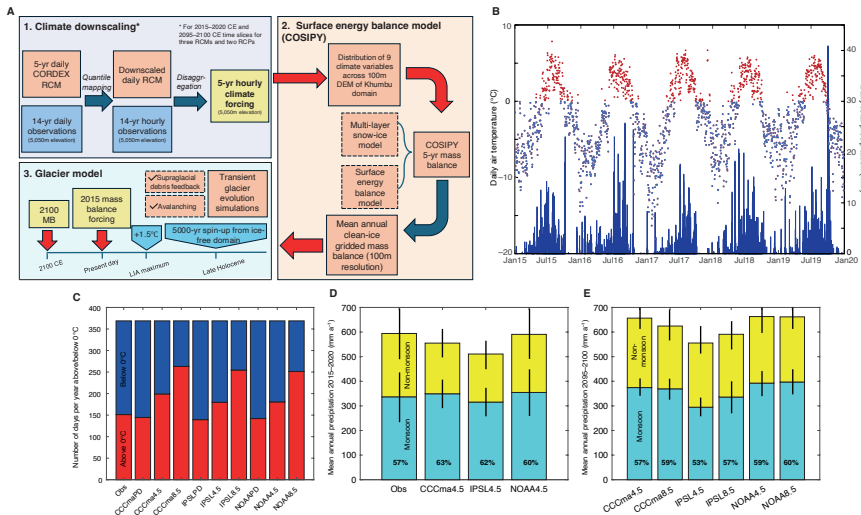
Figure 1: Khumbu Glacier location and context. (a) Map of High Mountain Asia showing the location of the monsoon-influenced Central and Eastern Himalaya and Khumbu Glacier. (b) hypsometry of glaciers and debris-covered glacier ice in the Central and Eastern Himalaya compared with the elevation range of Khumbu Glacier. (c) Map of Khumbu Glacier showing the glacier outline from the RGI database (black line) that is equivalent to the late Holocene (~1 ka) glacier extent identified from ice-marginal moraines, the hydrological catchment that represents the model domain (blue line), the extent of supraglacial debris, location of the Khumbu Icefall, the extent of active ice flow inferred from observations of glacier velocity, and location of the automatic weather stations (AWS) used for RCM downscaling (blue stars). (d) Estimated mass balance gradient for debris-covered glaciers in the Everest region (Benn and Lehmkühl, 2000) compared with the glacier mass balance gradient simulated using the NOAA RCM, and showing change in the equilibrium line altitude (ELA) of Khumbu Glacier in the historical and future simulations for the NOAA RCM RCP4.5 experiment.



Deleted: 

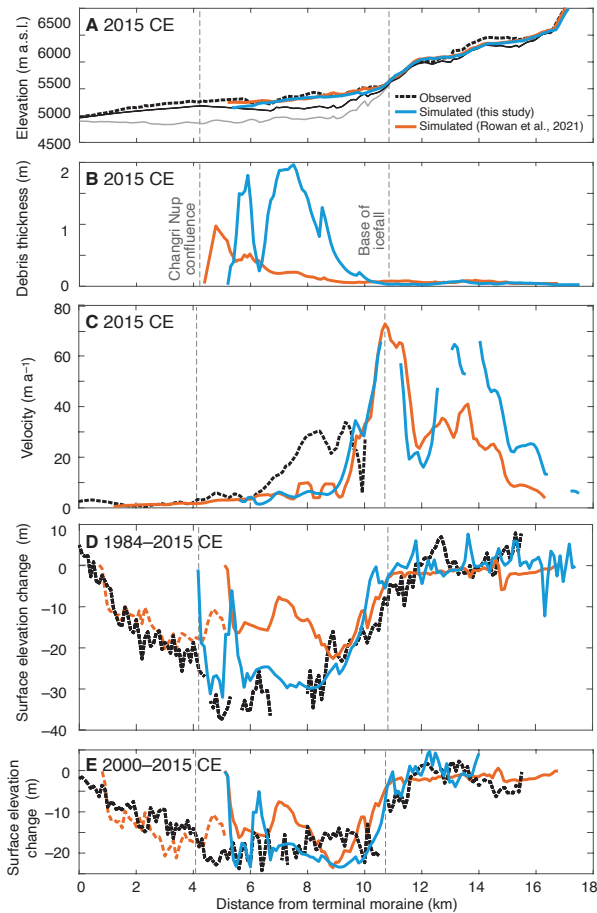
Formatted: Left

Deleted: Satellite image of 



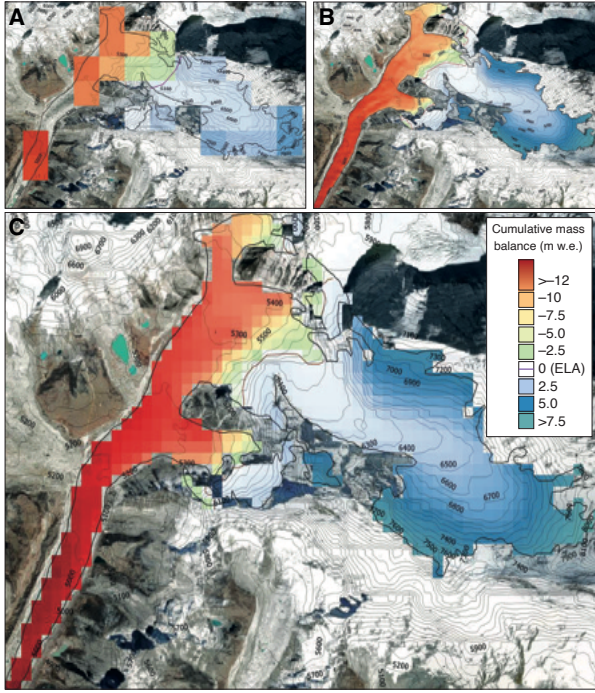
1386  
1387  
1388  
1389  
1390  
1391  
1392  
1393  
1394  
1395  
1396  
1397  
1398  
1399  
1400  
1401  
1402  
1403  
1404  
1405  
1406  
1407

Figure 2: Glacier model experimental design and evaluation of RCM downscaling. (a) Schematic diagram of the glacier modelling approach showing the methods used for downscaling through quantile mapping and disaggregation of climate data. Surface energy balance modelling using COSIPY includes the preprocessing stage of meteorological distribution across the Khumbu domain, which is repeated for each RCM in the 2015–2020 CE climates and for the three RCMs and two RCPs for the 2095–2100 CE climates. The simulated mass balances are then used to force the iSOSIA model. (b) Daily mean temperature and daily total precipitation from the NOAA RCM for the present day (2015–2020 CE) following downscaling using quantile mapping with air temperature categorised into above freezing (red) and below freezing (blue). (c) Proportion of air temperatures above and below freezing for the present day for each RCM and RCP for the downscaled daily data compared with observations. (d) Annual precipitation totals for non-monsoon and monsoon with standard deviation between selected years shown by black bars for the downscaled daily data compared with observations. (e) Future (2095–2100 CE) time-slice annual precipitation totals for non-monsoon and monsoon months with standard deviation between selected years shown by black bars. In (d) and (e) the percentage of the total annual precipitation occurring during the monsoon is indicated by the value in bold text. (Obs = meteorological observations from AWS).

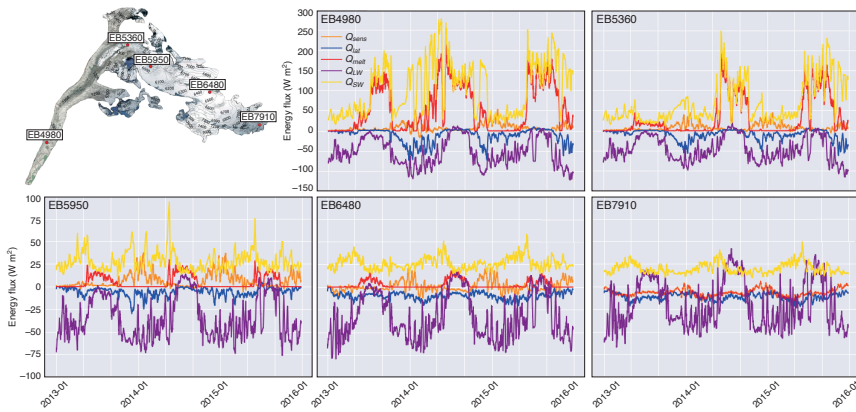


1408  
 1409  
 1410  
 1411  
 1412  
 1413  
 1414  
 1415  
 1416  
 1417  
 1418  
 1419  
 1420  
 1421  
 1422  
 1423  
 1424  
 1425

Figure 3. Evaluation of NOAA present-day simulation showing; (a) mean simulated glacier surface elevation and bed elevation calculated from a 500 m-wide swath profile along the central flowline of the glacier. Subglacial topography including the dynamically detached debris-covered tongue is shown by the solid black line and subglacial topography used in the entire glacier simulations in Rowan et al. (2015) is shown for comparison by the lowermost grey solid line. The estimated present-day ice surface elevation (Farinotti et al., 2019) is shown by the dashed black line. (b) mean simulated debris thickness, (c) simulated and observed velocities from the NASA MEaSURES ITS\_LIVE project (Dehecq et al., 2019), and simulated and observed mean surface elevation change between (d) 1984–2015 CE and (e) 2000–2015 CE using geodetic observations from King et al. (2020) compared with results from the simulations in this study and those in Rowan et al. (2021) where further information about the model evaluation can be found.

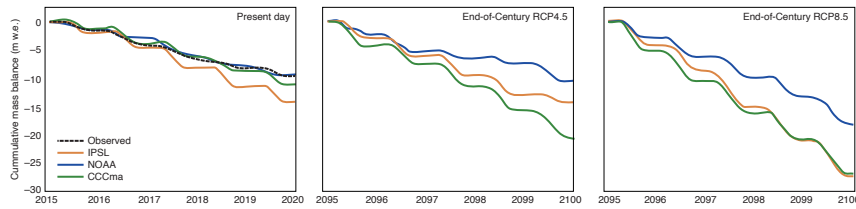


1426  
 1427  
 1428 Figure 4. COSIPY reference calculation of present-day mass balance for Khumbu Glacier for the period  
 1429 2013–2015 CE showing the results from calculations using different grid spacings using (a) a 1-km  
 1430 grid, (b) a 30-m grid, (c) the 200-m grid spacing used throughout the experiments in this study.  
 1431  
 1432  
 1433  
 1434  
 1435  
 1436  
 1437



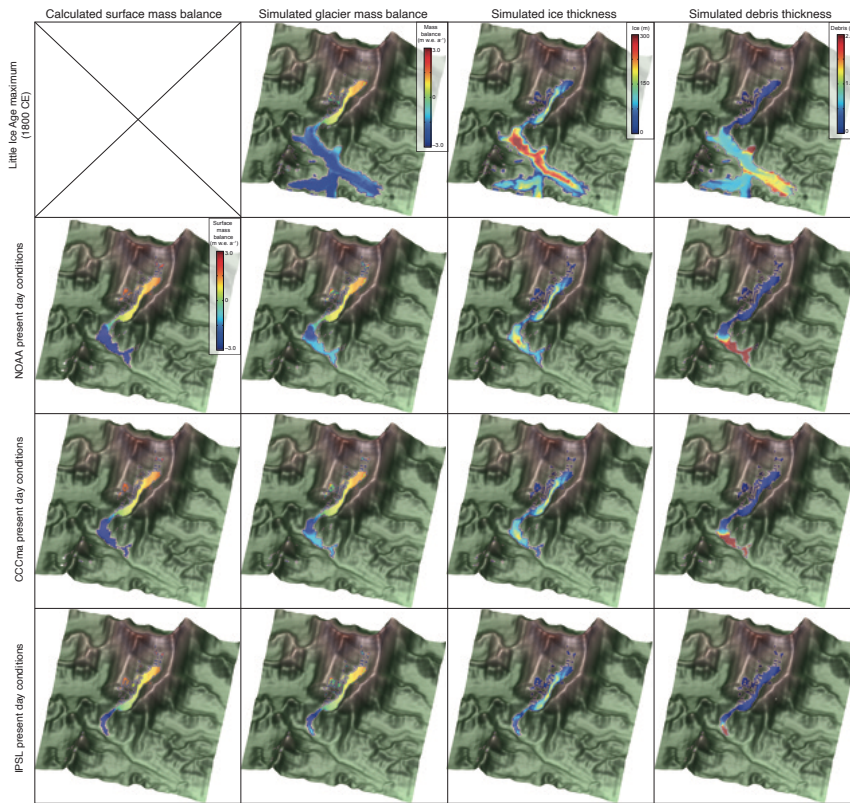
1438  
1439  
1440  
1441  
1442  
1443  
1444  
1445  
1446  
1447  
1448  
1449

Figure 5. Locations of energy balance calculation points used for energy flux and melt components analysis in the reference calculation and sensitivity tests (named after their corresponding altitude e.g., EB6480) showing 5-day average of energy fluxes across study period for each site. Note that scales for energy flux are different for the two sites below the icefall compared to the three sites above the icefall.



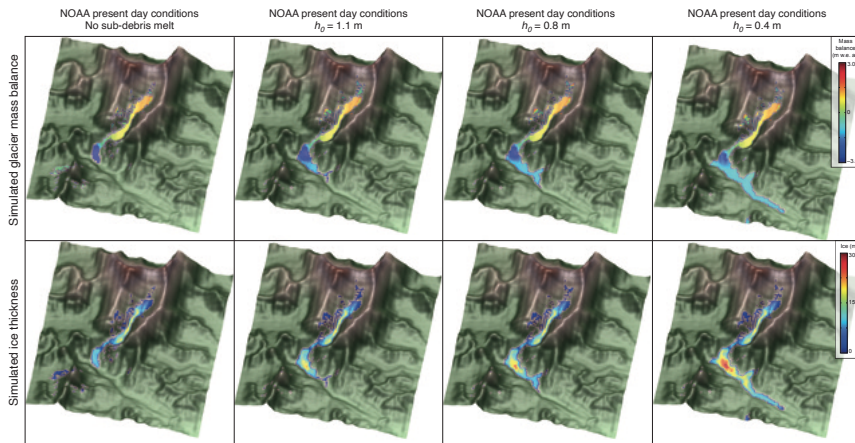
1450  
1451  
1452  
1453  
1454  
1455  
1456  
1457  
1458  
1459  
1460

Figure 6. Spatially averaged cumulative clean-ice mass balance with clear seasonality for the present day time slice including the mass balance forced by the observations used for downscaling, and the end-of-Century time slice under RCP4.5 and RCP8.5. The low annual glacier-wide mass balance values shown here result from the extent of the model domain used to force the glacier model that includes the larger catchment beyond the glacier margins and therefore contains a higher proportion of lower elevations than those of the glacier itself. However the similarity between the mass balance results for simulations forced by NOAA RCM and observations can be clearly seen, and the differences between the three RCMs is apparent in all time slices.



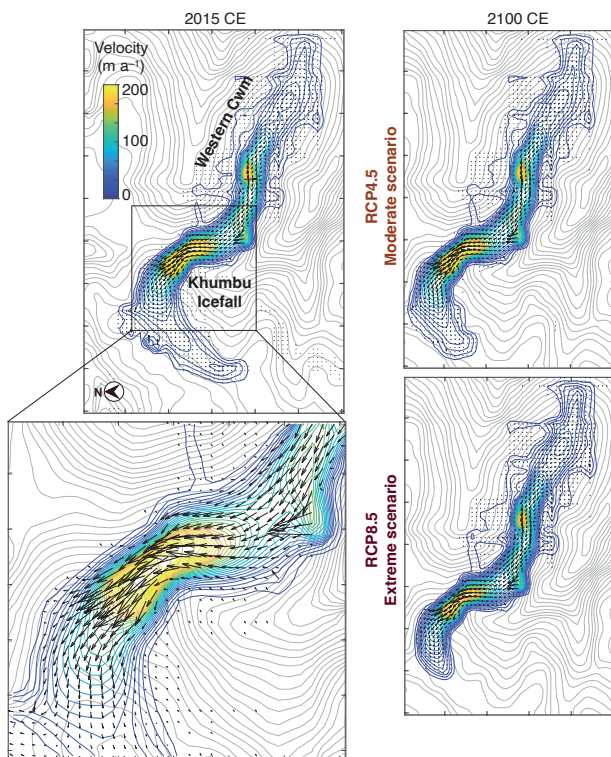
1461  
 1462  
 1463  
 1464  
 1465  
 1466  
 1467  
 1468  
 1469

Figure 7. iSOSIA model sensitivity to surface energy and mass balance forcing, showing ‘Little Ice Age’ (~1800 CE) maximum glacier mass balance, ice thickness and debris thickness. Present-day results for surface mass balance calculated using each RCM with COSIPY showing glacier mass balance calculated using the same climate forcing following integration with the glacier model, simulated ice thickness, and simulated debris thickness.



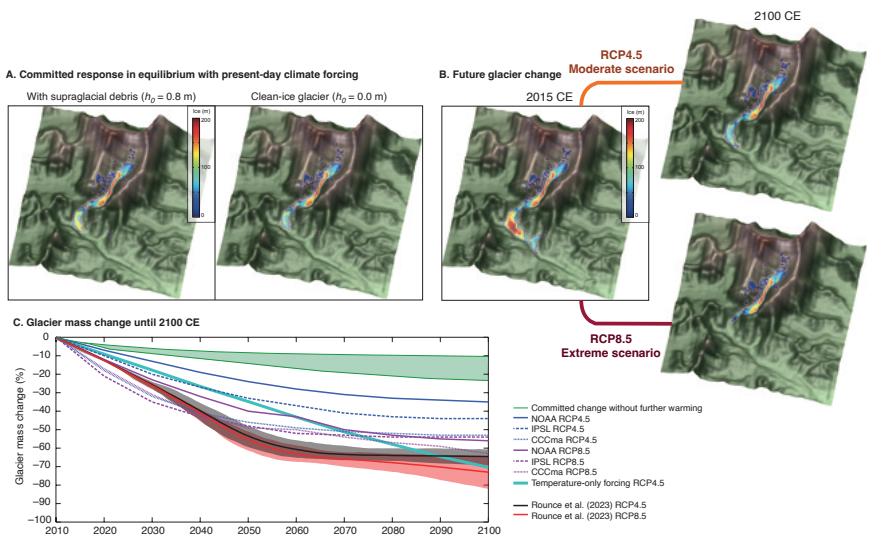
1470  
 1471  
 1472  
 1473  
 1474  
 1475  
 1476  
 1477  
 1478  
 1479  
 1480

Figure 8. Glacier mass balance and ice thickness simulated using the NOAA RCM climate forcing and the resulting simulated ice thickness where no sub-debris melt is imposed and the glacier has an entirely debris-free surface compared with ice results for simulations with  $h_0$  values of 0.4 m, 0.8 m, and 1.1 m where  $h_0$  is a constant in Equation (1) representing the characteristic debris thickness at which the reduction in ablation due to insulation by supraglacial debris is 50% of the value for an equivalent clean-ice surface (Anderson and Anderson, 2016; Rowan et al., 2021).



1481  
 1482  
 1483  
 1484  
 1485  
 1486  
 1487  
 1488  
 1489  
 1490  
 1491  
 1492

Figure 9. Simulated ice flow for Khumbu Glacier. Velocity-vector maps showing simulated ice flow magnitude and direction from the present day (2015–2020 CE) and 2100 CE under RCP4.5 and RCP8.5 using the downscaled NOAA climate forcing. Simulated ice flow speed is shown as colour shading with blue contours, and the bed topography is shown by grey contours. The outermost contour in each plot represents the slowest ice flow close to the glacier margins with depth-integrated velocities of 5–10 m a<sup>-1</sup>. Note that rapid flow across the Western Cwm indicated by a single arrow represents the effects of avalanching rather than sustained glacier flow.



1493  
1494  
1495  
1496  
1497  
1498  
1499  
1500  
1501  
1502  
1503  
1504  
1505  
1506

Figure 10. Future glacier volume change projections until 2100 CE. (a) Equilibrium ice thickness accounting for the committed response to recent climate change using the downscaled NOAA RCM climate forcing with and without the effect of supraglacial debris on mass balance. (b) Simulated ice thickness under RCP4.5 and RCP8.5 for 2100 CE using the downscaled NOAA RCM climate forcing. (c) Comparison of projected shrinkage of Khumbu Glacier by 2100 CE from this study with those from Rounce et al. (2023) showing results from each of the six experiments in this study with results from RCP4.5 and RCP8.5 from Rounce et al. (2023), the equivalent result for a simulation using a change in MAAT equivalent to the NOAA RCP4.5 forcing where precipitation does not change from the present-day value (cyan line). The green shading shows the range of the committed volume loss due to historical warming.

1507 **Appendix**

1508 This appendix contains further details on the meteorological data collection and analysis, RCM  
1509 downscaling, evaluation of the present-day downscaled RCM results using meteorological data and the  
1510 distribution of these results across the model domain, and the parameterisation and sensitivity testing  
1511 of the COSIPY model. The Indian Summer Monsoon season was defined as June to October, the post-  
1512 monsoon as October–November, winter as December–February, and the pre-monsoon as March–May  
1513 (Ueno et al., 2008). Although much of this study compares the monsoon season against the non-  
1514 monsoon season, it should be noted that the timing of monsoon onset and cessation can vary between  
1515 years. Day time was defined as 08:00–16:00 and night as 20:00–04:00 (Nepal local time) to account for  
1516 changing sunrise and sunset times throughout the year and the influence of topographic shading in the  
1517 valleys; centred-means were used for some datasets to remove local noise associated with daily  
1518 frequencies. For sub-hourly measurements, hourly averages were calculated using data from the  
1519 previous hour. The period for the reference simulation and sensitivity experiments was January 1<sup>st</sup> 2013  
1520 to December 31<sup>st</sup> 2015. RCM downscaling to produce the five-year time slices represented the periods  
1521 January 1<sup>st</sup> 2015 to December 31<sup>st</sup> 2019 and January 1<sup>st</sup> 2095 to December 31<sup>st</sup> 2099.  
1522

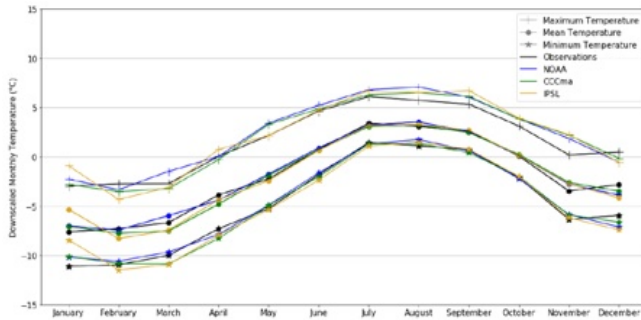
1523 **A1. Gap filling of the AWS data**

1524 All AWS datasets contained periods of erroneous measurements and missing data, which is unsurprising  
1525 given the challenges of maintaining equipment in such an environment (Oulkar et al., 2026). Daily air  
1526 temperature averages were calculated when 83% (20 hours) of observations were available. For  
1527 calculation of lapse rates for longer time periods (e.g. daytimes during the monsoon season) the  
1528 distributions of missing data across these periods were analysed. For example, the Lukla AWS had  
1529 almost 45% of temperature observations missing during the monsoon season but as these were equally  
1530 distributed between day and night, lapse rates could be calculated using station pairs following the  
1531 method of Immerzeel et al. (2014). Up to 13% of the West Changri Nup AWS temperature records were  
1532 missing, and these were interpolated using the Ev-K2-CNR Pyramid AWS data with the same lapse rate  
1533 as the GlacioClim dataset. The interpolated results were compared with the preceding and succeeding  
1534 periods from the same AWS, and the preceding and succeeding months from other AWS, and compared  
1535 with data collected in November 2014 at the GlacioClim North Changri Nup AWS (5,470 m a.s.l.).  
1536

1537 Data gaps in the precipitation datasets were significant, particularly during the onset of the monsoon  
1538 (e.g., 45% of data points were missing for the Namche AWS) meaning the altitudinal dependency of  
1539 precipitation could not be fully characterised. This led to several monsoon seasons with little or no data  
1540 at individual AWS. Given that the aim of this study was to analyse *in situ* trends, gap-filling through  
1541 interpolation was not conducted for these AWS during the seasons without data. Station pairs were used  
1542 to determine the elevation dependency of precipitation for the reference simulation following the  
1543 method of Immerzeel et al. (2014). Results from the Kala Patthar/Pheriche station pair and the  
1544 Pyramid/Pheriche station pair in 2009, and the Kala Patthar/Namche station pair during 2011, show that  
1545 the relationship between precipitation amount and elevation was more negative during the monsoon  
1546 season ( $-0.011\% \text{ m}^{-1}$  to  $-0.018\% \text{ m}^{-1}$ ) than during the non-monsoon ( $-0.0039\% \text{ m}^{-1}$  to  $-0.0043\% \text{ m}^{-1}$ ).  
1547 No interpolation to fill data gaps was required for other meteorological variables, apart from albedo  
1548 but as this was only measured at the West Changri Nup AWS there was no suitable surrogate for this  
1549 variable.  
1550

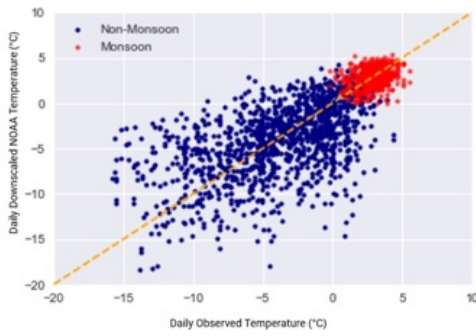
1551 **A2. Downscaled climate model results compared with observations**

1552  
1553



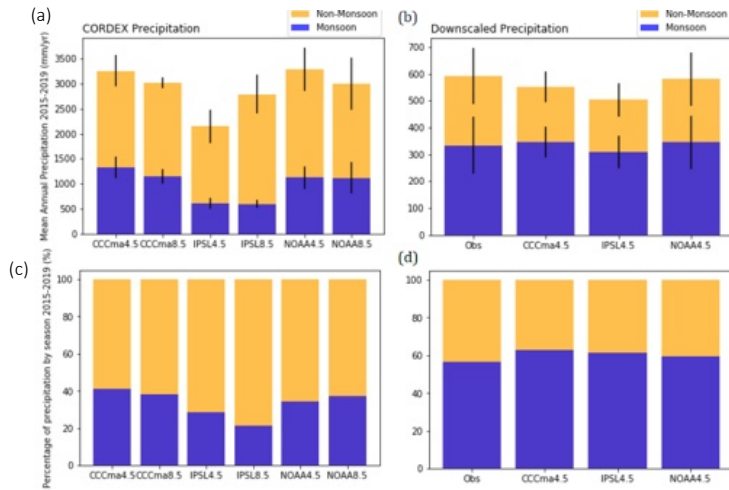
1554  
1555  
1556  
1557  
1558  
1559  
1560  
1561  
1562

Figure A1: Downscaled monthly mean, maximum, and minimum temperature calculated for the present day time slice compared with observations from the GlacioClim Pyramid Observatory AWS.



1563  
1564  
1565  
1566  
1567  
1568  
1569  
1570  
1571

Figure A2: Daily downscaled temperature from the NOAA RCM against observations from the GlacioClim Pyramid Observatory AWS split by monsoon/non-monsoon. The 1:1 relationship is shown by the dashed orange line.

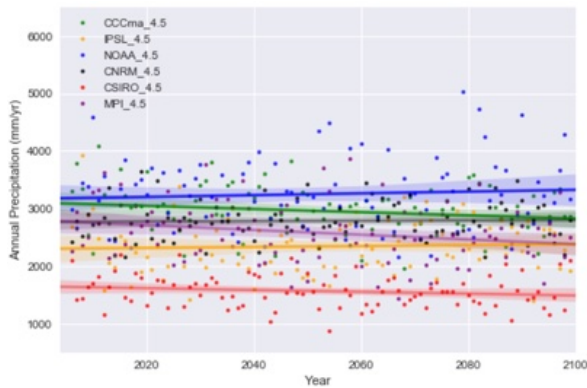


1572  
1573  
1574  
1575  
1576  
1577  
1578  
1579  
1580  
1581  
1582  
1583  
1584  
1585  
1586  
1587

Figure A3. Annual precipitation totals for the monsoon and non-monsoon seasons. (a and b) Precipitation totals before and after downscaling, with the standard deviation between selected years shown by black bars. (c and d) The same results as seasonal percentages. The annual precipitation is in good agreement with measurements in the southern Dudh Koshi catchment for the gridbox nearest to Khumbu Glacier is located at 27.9065056°N, 86.4352951°E at 2,100 m a.s.l..

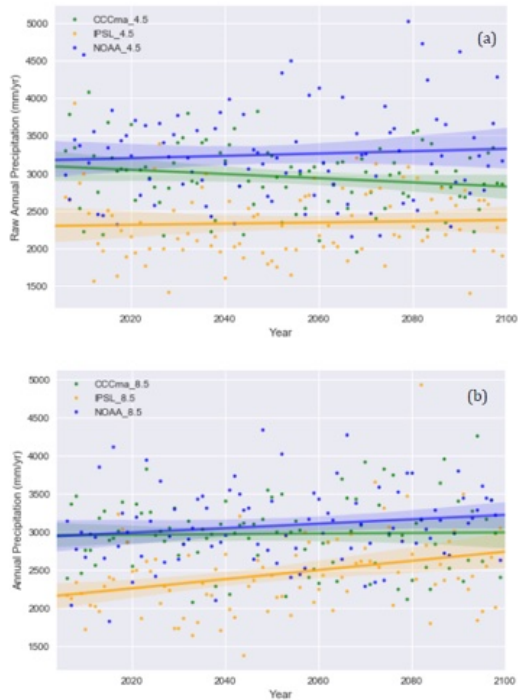
**A3. Regional Climate Model analysis and selection**

Three of the six available CORDEX South Asia RCMs (NOAA, CCCma, IPSL) were selected as discrete scenarios that spanned the range of possible future precipitation conditions (Table 1); either wet, moderate, or dry climate in 2080–2100 CE (Fig. A4). The raw RCMs significantly overestimated the annual total precipitation by at least a factor of five for the selected gridpoint, which was corrected by downscaling of these results using the AWS data.



1588  
1589  
1590  
1591  
1592

Figure A4: Annual precipitation sums (dots) with fitted trend line from the start of the RCP experiments (2006–2100 CE) for each of the six Indian Institute for Tropical Meteorology CORDEX models for RCP4.5.



1593  
 1594  
 1595 Figure A5: Annual precipitation sums (dots) with fitted trend line from the start of the RCP experiments  
 1596 (2006–2100 CE) for the three selected of the six CORDEX models for (a) RCP4.5 and (b) RCP8.5.  
 1597  
 1598

1599 **A4. Downscaling parameters and method**

1600 While minimum and maximum air temperatures are not required to as inputs to COSIPY, these were  
 1601 downloaded and statistically downscaled using quantile mapping with normal distribution to aid  
 1602 disaggregation to an hourly time step using MELODIST (Table A1). Quantile mapping for the  
 1603 CORDEX wind speed data was found to be ineffective when analysing the time series output against  
 1604 observations, both for the absolute wind speed as well as the reduced day-on-day variability seen during  
 1605 the monsoon season, and therefore, GARD was used instead. This is a simple statistical analogue  
 1606 regression downscaling method appropriate for pointwise downscaling.  
 1607  
 1608  
 1609

Table A1: RCM-derived parameters and the method used for downscaling or bias correction.

RCM-derived parameters	Downscaling/bias correction method	Parametric distribution model (for Quantile mapping)	References
Precipitation (kg per m <sup>2</sup> per s, converted to mm day <sup>-1</sup> )	Quantile mapping	Gamma	Vrac et al., 2007; Piani et al., 2010
Mean temperature (K) Minimum temperature (K) Maximum temperature (K)	Quantile mapping	Normal / Gaussian	Li et al., 2010, Gupta et al., 2016; Luo et al., 2018
Incoming shortwave (W m <sup>-2</sup> ) Incoming longwave (W m <sup>-2</sup> )	Quantile mapping	Beta	Ruane et al., 2015

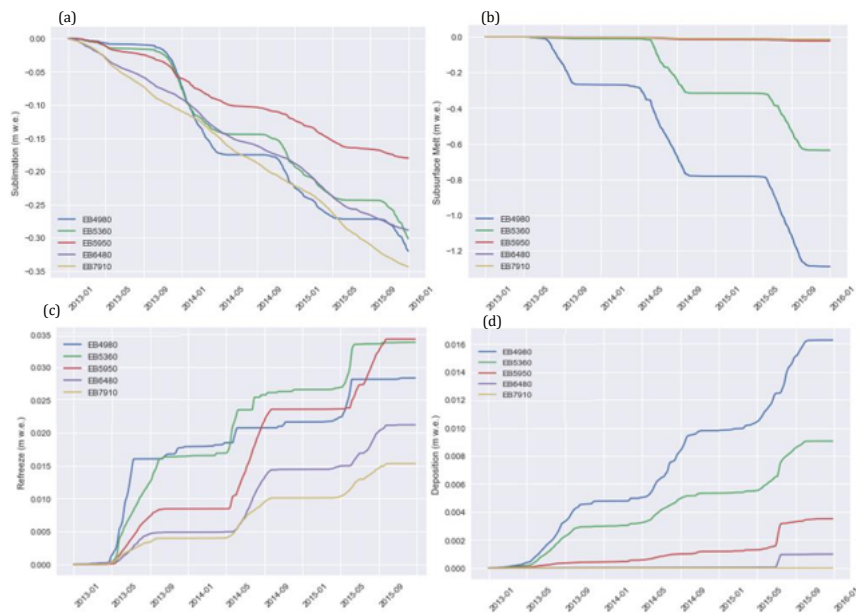
Relative humidity (%)			
Pressure (hPa)	Bias correction	N/A	N/A
Wind speed (m s <sup>-1</sup> )	Regression downscaling	N/A	Gutmann et al., 2022

1610  
1611  
1612  
1613  
1614  
1615  
1616  
1617  
1618  
1619  
1620  
1621  
1622  
1623  
1624  
1625  
1626  
1627  
1628  
1629  
1630  
1631  
1632  
1633  
1634  
1635

#### A5. Variability in surface energy balance with elevation

The contributions of the components of the surface energy balance were tested at five points along the glacier centreline (Fig. 5) and found to vary substantially in both absolute values and seasonality. Net shortwave radiation ( $Q_{sw}$ ) contributed the largest energy input to the glacier surface at the lower elevation sites and correlated most strongly with  $Q_{melt}$ . The high temporal variability related to varied cloud cover and fluctuating albedo during the warmer months with the melting of the snowpack.  $Q_{sw}$  was low at higher elevations, but high  $SW_{in}$  at the higher sites indicates that this is not due to topographic shading.  $Q_{sw}$  is correlated with albedo, and the persistence of snow throughout much of the year will reduce  $Q_{melt}$ .  $Q_{LW}$  rose above zero during the monsoon season at sites EB5950, EB6480 and EB7910, mostly due to heavy cloud cover and increased temperatures relative to the glacier surface.  $Q_{lat}$  was close to zero at the lower elevation sites as the arrival of the monsoon led to higher relative humidity, and this pattern was similar but dampened at higher elevations. At the highest site, EB7910,  $Q_{melt}$  correlated exactly with the sensible heat flux.

Sublimation occurred at all elevations, with the highest cumulative loss at EB7910 (Fig. A6A). Sublimation rates correlated with seasonality down-glacier; at EB7910 sublimation only slightly slowed from December until May, while sublimation at site EB4980 increased from April until the start of the monsoon in July. Subsurface melt at or above the ELA (5,950 m a.s.l.) was negligible, but lower elevation sites showed stronger seasonal cycles related to surface temperatures. Refreezing (Fig. A6C) occurred at all sites and the onset of refreezing was staggered with increasing elevation, although absolute values remained low. Higher  $Q_{lat}$  during the monsoon resulted in higher deposition of snow to the glacier at lower elevations and negligible rates at higher elevations. Similar absolute values and patterns are seen for condensation (results not shown).



1636  
1637  
1638  
1639  
1640  
1641  
1642

Figure A6. 5-day averages of (a) sublimation, (b) subsurface melt, (c) refreeze, and (d) deposition for the five surface energy balance sensitivity testing sites across Khumbu Glacier (see Fig. 5 for locations of these sites).

#### 1643 A6. COSIPY parameter testing and sensitivity results

1644 To isolate the impact of individual surface energy balance variables on the mass balance of Khumbu  
1645 Glacier, each variable was perturbed individually, and air temperature and precipitation amount were  
1646 tested in tandem for the reference period 2013–2015 CE (Table A2). Perturbations of all variables were  
1647 within the range of possible uncertainty that arise from a combination of observations, climate models,  
1648 downscaling approach or the distribution of meteorology. The positive temperature and precipitation  
1649 perturbations were in the order of possible future climate forcings. The spatially averaged mass balance  
1650 was most sensitive to changes in  $LW_{in}$ , air temperature, and  $SW_{in}$ , and relative humidity had the least  
1651 impact on ablation/accumulation rates (Fig. A7). The coupled parameter testing (Fig. A8) perturbed  
1652 precipitation and air temperature simultaneously. The most significant change in spatially averaged  
1653 mass balance followed a 3°C increase in air temperature and 20% decrease in precipitation amount. The  
1654 increase in ablation following an increase in air temperature of 1.5°C was completely compensated by  
1655 the increase in accumulation resulting from a 20% increase in precipitation amount.

1656 Accurate estimation of precipitation phase is important for summer-accumulation type glaciers and  
1657 threshold values of air temperature are often used to separate liquid and solid precipitation. Previous  
1658 work calculated threshold temperatures across 6,883 AWS in the Northern Hemisphere to find an  
1659 average rain/snow partitioning value of 1°C, with 95% of observations falling between 0.4°C and 2.4°C  
1660 (Jennings et al., 2018). Although there remains a lack of such data for High Mountain Asia, Jennings et  
1661 al. (2018) found that high mountain areas have the highest rain/snow partitioning thresholds, with a  
1662 value of up to 4.5°C on the Tibetan Plateau. The impact of two different precipitation partitioning  
1663 schemes on glacier mass balance was investigated here. Threshold temperatures of 0.5°C, 2.0°C and  
1664

1665 3.5°C were chosen and compared with the default value in COSIPY (STF), and a scheme that smoothly  
 1666 scaled from 100% solid precipitation at -1°C to 0% solid precipitation at 4°C was also tested.  
 1667

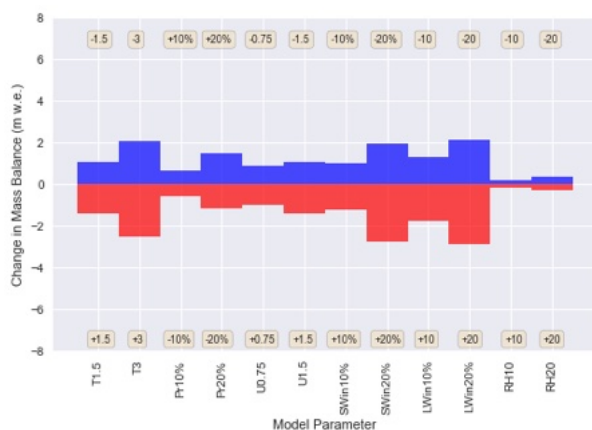
1668 The glacier ice surface roughness ( $z_0$ ) was defined as 1.7 mm for the reference simulation, which is a  
 1669 reasonable estimate for clean-ice glaciers (Mölg et al., 2012). The  $z_0$  values reported within the literature  
 1670 vary widely for clean-ice glaciers, and two substantially different  $z_0$  values were tested. A  $z_0$  value of  
 1671 0.1 mm was measured at Midtre Lovénbreen, Svalbard (Irvine-Fynn et al. 2014), and August-One  
 1672 glacier, China (Guo et al., 2018), and a  $z_0$  value of 6.9 mm was calculated on the clean-ice section of  
 1673 the Haut Glacier D’Arolla (Brock et al., 2006) and Laohugou Glacier No. 12 (Sun et al., 2018). These  
 1674 values were used as endmembers of the likely range in values for Khumbu Glacier. The  $z_0$  value had  
 1675 minimal impact on glacier mass balance (Fig. A9) although a higher (lower) value for  $z_0$  did result in  
 1676 slightly increased (decreased) mass balance. The mass balance sensitivity was not proportional to the  
 1677 change in  $z_0$ , with a  $z_0$  value of 1.6 mm lower than the reference value leading to a similar mass balance  
 1678 change than that of the experiment with a  $z_0$  value of 5.2 mm higher than the reference value.  
 1679

1680 The albedo values of the three glacier components were perturbed by  $\pm 0.05$  from that used in the  
 1681 reference experiment (e.g., 0.85 for fresh snow). There was a strong response of the glacier mass balance  
 1682 to changing snow albedo. Reducing snow albedo by 0.05 led to a 65% reduction in mass balance of  
 1683 2.21 m w.e. (Fig. A9). Ablation (accumulation) rates were 3.7 m w.e. (1.75 m w.e.) higher relative to  
 1684 the reference simulation for this perturbation. This result further supports the importance of  $Q_{SW}$  to  
 1685 ablation rates. Varying albedo values for firn and ice also revealed a lower sensitivity of glacier mass  
 1686 balance relative to snow albedo.  
 1687

1688 Table A2. Parameter perturbations for the sensitivity experiments. Note that for relative humidity the %  
 1689 refers to the units and not the perturbation.  
 1690

Parameter	Perturbation
Mean annual air temperature (C)	$\pm 1.5, \pm 2.0, \pm 3.0$
Precipitation amount (%)	$\pm 10, \pm 20, \pm 30$
Wind speed ( $\text{m s}^{-1}$ )	$\pm 0.75, \pm 1.5$
$SW_{in}$ and $LW_{in}$ (%)	$\pm 10, \pm 20$
Relative Humidity (%)	$\pm 10, \pm 20$

1692



1693

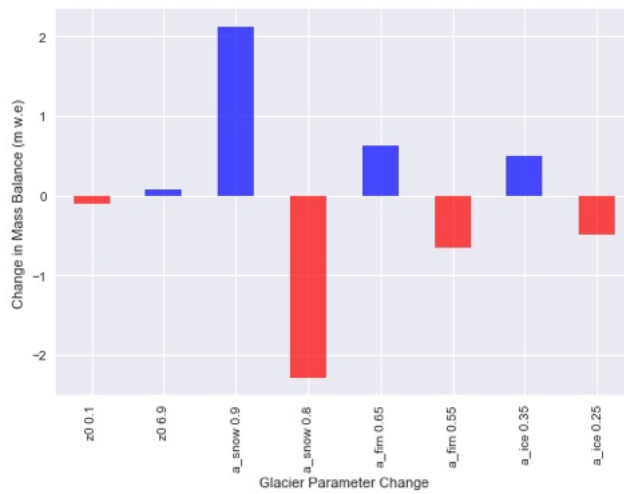
1694

1695 Figure A7. Single parameter sensitivity test results for reference simulation period 2013–2015 CE.



1696  
1697  
1698  
1699  
1700  
1701  
1702

Figure A8. Coupled parameter sensitivity test results for mean annual air temperature and precipitation amount for reference simulation period 2013–2015 CE.



1703  
1704  
1705  
1706  
1707  
1708  
1709  
1710  
1711  
1712

Figure A9. Sensitivity of mass balance for the reference simulation period 2013–2015 CE to changing glacier parameters (surface roughness, and albedo of snow, firm, and ice).

1713 **Additional references for Appendix A**

1714 Gupta, A. and Tarboton, D.G.: A tool for downscaling weather data from large-grid reanalysis products  
 1715 to finer spatial scales for distributed hydrological applications. *Environmental Modelling &*  
 1716 *Software*, 84, pp. 50–69. <https://doi.org/10.1016/j.envsoft.2016.06.014>, 2016  
 1717 Deleted: 2016

1718 Gutmann, E. D., J. J. Hamman, M. P. Clark, T. Eidhammer, A. W. Wood, and J. R. Arnold: En-GARD:  
 1719 A Statistical Downscaling Framework to Produce and Test Large Ensembles of Climate  
 1720 Projections. *J. Hydrometeorol.*, 23, 13545–1561, <https://doi.org/10.1175/JHM-D-21-0142.1>, 2022  
 1721 Deleted: .

1722 Immerzeel, W., Petersen, L., Ragettli, S. and Pellicciotti, F.: The importance of observed gradients of  
 1723 air temperature and precipitation for modelling runoff from a glacierized watershed in the  
 1724 Nepalese Himalayas. *Water Resources Research*. 50: 2212-2226. doi: 10.1002/2013WR014506,  
 1725 2013  
 1726 Deleted: .

1727 Jennings, K. S., Winchell, T. S., Livneh, B., and Molotch, N. P.: Spatial variation of the rain–snow  
 1728 temperature threshold across the Northern Hemisphere, *Nat Commun*, 9, 1148,  
 1729 <https://doi.org/10.1038/s41467-018-03629-7>, 2018.

1730 Lente, G. and Ósz, K.: Barometric formulas: various derivations and comparisons to environmentally  
 1731 relevant observations. *ChemTexts*, 6, pp.1-14. <https://doi.org/10.1007/s40828-020-0111-6>, 2020  
 1732 Deleted: ., 2020.

1733 Li, H., Sheffield, J. and Wood, E.F.: Bias correction of monthly precipitation and temperature fields  
 1734 from Intergovernmental Panel on Climate Change AR4 models using equidistant quantile  
 1735 matching. *Journal of Geophysical Research: Atmospheres*, 115(D10),  
 1736 <https://doi.org/10.1029/2009JD012882>, 2010  
 1737 Deleted: .

1738 Oulkar, S. N., Peacey, M. W., Mitrev, M., Quincey, D. J., Hubbard, B., Matthews, T., Oulkar, A. S.,  
 1739 Miles, K. E., and Rowan, A. V.: Design and implementation of a robust data logging and satellite  
 1740 telemetry system for remote cryospheric research, *Geosci. Instrum. Method. Data Syst.*, 15, 75–  
 1741 88, <https://doi.org/10.5194/gi-15-75-2026>, 2026.

1742 Ruane, A. C., Goldberg, R., and Chryssanthacopoulos, J.: Climate forcing datasets for agricultural  
 1743 modeling: Merged products for gap-filling and historical climate series estimation, *Agricultural*  
 1744 *and Forest Meteorology*, 200, pp. 233–248. <https://doi.org/10.1016/j.agrformet.2014.09.016>,  
 1745 2015  
 1746 Deleted: 2015.

1747 Salerno, F., Guyennon, N., Thakuri, S., Viviano, G., Romano, E., Vuillermoz, E., Cristofanelli, P.,  
 1748 Stocchi, P., Agrillo, G., Ma, Y., and Tartari, G.: Weak precipitation, warm winters and springs  
 1749 impact glaciers of south slopes of Mt. Everest (central Himalaya) in the last 2 decades (1994–  
 1750 2013), *The Cryosphere*. 9: 1229-1247. doi: 10.5194/tc-9-1229-2015, 2015,  
 1751 Deleted: (2015).

1752 Sun, W., Qin, X., Wang, Y. et al. The response of surface mass and energy balance of a continental  
 1753 glacier to climate variability, western Qilian Mountains, China. *Clim Dyn* 50, 3557–3570,  
 1754 <https://doi.org/10.1007/s00382-017-3823-6>, 2018  
 1755 Deleted: .

1756 Vrac, M., Stein, M.L., Hayhoe, K. and Liang, X.Z.: A general method for validating statistical  
 1757 downscaling methods under future climate change. *Geophysical Research Letters*, 34(18).  
 1758 <https://doi.org/10.1029/2007GL030295>, 2007  
 1759 Deleted: (2018).

1760 Wohlfahrt, G., Hammerle, A., Haslwanter, A., Bahn, M., Tappeiner, U. and Cernusca, A.: Disentangling  
 1761 leaf area and environmental effects on the response of the Net Ecosystem Co2 Exchange to  
 1762 diffuse radiation, *Geophysical Research Letters*, 35(16). doi:10.1029/2008gl035090, 2008.  
 1763 Deleted: .

1764 Wohlfahrt, G., Hammerle, A., Niedrist, G., Scholz, K., Tomelleri, E. and Zhao, P.: On the energy balance  
 1765 closure and net radiation in complex terrain, *Agricultural and Forest Meteorology*, 226–227, pp.  
 1766 37–49. doi:10.1016/j.agrformet.2016.05.012, 2016.  
 1767 Deleted: 2016

1768 Yang, K., N. Guyennon, L. Ouyang, L. Tian, G. Tartari, and F. Salerno: Impact of summer monsoon on  
 1769 the elevation-dependence of meteorological variables in the south of Central Himalaya.  
 1770 *International Journal of Climatology*. 5293: 1748-1759. doi:10.1002/joc.5293, 2017.  
 1771 Deleted: (2017).